Measurement 227 (2024) 114207

Contents lists available at ScienceDirect

Measurement

journal homepage: www.elsevier.com/locate/measurement

Dynamic image segmentation and recognition measurement of axial compression experiment based on image clustering and semantic segmentation in RC column with FRP tubes

Yankang Zhai [a,b], Alex Hay-Man Ng [a,c,*], Zhenpeng Luo [a], Jiahui Wang [a], Lijuan Li [a], Zhe Xiong [a], Hua Wang [d]

[a] School of Civil and Transportation Engineering, Guangdong University of Technology, Guangzhou 510006, China
[b] School of Information Engineering, Guangdong University of Technology, Guangzhou 510006, China
[c] Key Laboratory for City Cluster Environmental Safety and Green Development of the Ministry of Education, Guangdong University of Technology, Guangzhou 510006, China
[d] College of Resources and Environment, South China Agricultural University, Guangzhou 510000, China

ARTICLE INFO

Keywords:
Image Vision Measurement
Reinforced Concrete (RC) Column with Fiber Reinforced Polymer (FRP) Tubes
Axial Compression Experiments
Clustering Segmentation
Semantic Segmentation
RLOWESS and Time Filtering

ABSTRACT

This paper introduces a dynamic image recognition and measurement method for Reinforced Concrete (RC) Column with Fiber Reinforced Polymer (FRP) tubes axial compression experiments based on image segmentation, which includes two image processing modes: clustering segmentation and semantic segmentation. The method uses image processing techniques to extract and segment the deformation of RC column with FRP tube in the axial compression experiment, enabling tracking and measurement of the axial deformation process. Both visual segmentation methods have undergone a series of processes including image preprocessing, image segmentation, deformation tracking measurement, system optimization, and deformation comparison and validation analysis. In order to evaluate the performance of the proposed method, the measurements obtained from the proposed methods are compared with the one using the linear variable differential transformer (LVDT). An experiment has been conducted with 9 groups in RC column with FRP tube to assess the performance of the proposed methods. The comparison with the LVDT measurements shows that standard deviation of the average maximum offset measured by the K-means clustering algorithm is 1.65 mm, and the mean relative error of measurement is 1.03 %; while the standard deviation of the average maximum offset measured by the U-Net semantic segmentation algorithm is 0.95 mm, and the mean relative error of measurement is 0.44 %. The results suggest that the U-Net semantic segmentation algorithm perform slightly better than the K-means clustering algorithm in deformation tracking measurement. Even in circumstances where traditional LVDT measurements failure due to equipment malfunctions or exceeding the measurement limits, the visual displacement measurement methods are still capable for providing consistent and reliable displacement data. In cases of human occlusion issues within the video, correction can be implemented using outlier frame removal techniques. Moreover, the visual measurement techniques are capable of distinguishing the deformation directions, i.e. deformation towards east or vice versa. The proposed method has potential application value in practical engineering applications and can provide effective technical support for axial compression experiments and deformation monitoring of reinforced concrete structures.

1. Introduction

In the past decades, structural health monitoring has mainly relied on conventional sensor technologies such as linear variable differential transformer (LVDT). In the experiments of compressive and tensile testing of reinforced concrete (RC) column with FRP (Fiber Reinforced Polymer) tube specimens, the displacement of the columns provides valuable information about the failure modes of the specimens [1,2]. For this reason, the LVDT [3,4] is extensively employed to measure the deformation of concrete specimens, since the displacement information can provide valuable insights into the deformation mechanisms of RC

* Corresponding author.
E-mail address: hayman.ng@gmail.com (A.H.-M. Ng).

https://doi.org/10.1016/j.measurement.2024.114207
Received 20 September 2023; Received in revised form 3 January 2024; Accepted 19 January 2024
Available online 26 January 2024

Nomenclature

RC	Reinforced Concrete
FRP	Fiber Reinforced Polymer
LVDT	The Linear Variable Differential Transformer
RLOWESS	Robust Locally Weighted Regression
DIC	Digital Image Correlation
FEM	Finite Element Method
PSP	Pressure-Sensitive Paint
LiDAR	Light Detection and Ranging
SEM	Scanning Electron Microscope
ROIs	Region of Interests
RGB	Red, Green, Blue
LAB	CIE-LAB (Commission Internationale de l'Eclairage - LAB)
XYZ	CIE-XYZ (Commission Internationale de l'Eclairage - XYZ)
FPS	Frame Per Second

specimens [5–7]. While the LVDT is widely accepted as the conventional method for measuring displacement in concrete specimens, it has several limitations in measuring various deformation components. In practical experiments, the measurement of object deformation through LVDT requires the use of embedded device systems for signal acquisition. However, the implementation of such systems introduces complexities in terms of installation and wiring. Choosing an incorrect measuring range or inadequate fixation of the LVDT can lead to distortion in the measured data [8]. Therefore, it is often challenging when dealing with varying sizes of RC column with FRP tube, as it is necessary to select the LVDT with measuring ranges that area appropriate for the specific dimensions of the columns. Furthermore, it should be noted that the LVDT is limited in their ability to measure only measure specific points, resulting in a scarcity and inadequacy of global measurements. Improper usage and fixation of the LVDT can also result in detachment issues. Due to these problems, there is a need to develop advanced methods for accurate and efficient deformation measurements.

With the continuous advancement of computer science and image processing techniques, researchers are adopting digital image processing methods for acquiring more comprehensive structural information. Techniques such as Digital Image Correlation (DIC) [9,10], image-based 3D reconstruction [11,12], and computer vision motion-related [13,14] methods have gained widespread use for their effectiveness. Example of applications include Lin's use of micro DIC for specimen crack measurement [15], Zhou's employment of SEM for sample movement misalignment movement measurement [16], Dong's integration of Pressure-Sensitive Paint (PSP) with stereoscopic image correlation for wind tunnel deformation measurements [17], Zhu's implementation of image feature enhancement for displacement measurements [18], and Fang's application of LiDAR-based U-Net network for landslide deformation analysis [19].

Currently, image vision-based methods for time-series deformation measurement are increasingly becoming a mainstream technique in visual analysis. The use of vision-based measurement techniques has provided greater potential in capturing full-field deformation information. These detailed measurements offer a more comprehensive understanding of the deformation phenomena, which is crucial for testing, evaluation, and analysis of experimental outcome. For example, inverse analysis is a promising method in the field of material characterization, which heavily relies on full-field data, for example, global displacement provides high-fidelity experimental data, and when combined with the finite element method (FEM), it forms the DIC-FEM inversion method, which better explains the complex mechanical properties of materials [20]. However, in the experimental application of RC column with FRP tube currently lacks of integration techniques for image recognition, segmentation, and measurement. To address the challenge of identifying and measuring the external appearance of glass fibers without using DIC due to its processing limitations under complicated background, a possible approach is to utilize image segmentation methods.

Segmentation-based measurement is an important branch within the field of visual measurement. Within this field, color-based clustering segmentation and semantic image segmentation are the two commonly employed image segmentation methods. Color-based clustering segmentation provides a starting point for effectively identifying and segmenting objects such as glass fibers based on their unique color characteristics [21–23]. Semantic segmentation method, such as the U-Net [24], which commonly employed in medical image segmentation, can be adapted and trained for semantic segmentation-based measurement [25,26], expanding the application of these methods to this work.

The K-means clustering algorithm, a color-based clustering segmentation method, has been widely applied in the optimization and iterative refinement of image segmentation [27,28]. The successful utilization of K-mean clustering algorithm has been demonstrated in various related applications, for example, the K-means algorithm can be used to achieve the identification of concrete aggregates in low-contrast scanning electron microscope (SEM) or microscope images [29]; Using K-means clustering segmentation technique to classify fruits and determine their freshness is a common application method [30]. The algorithm has great potential to be used for applications in non-contact structural monitoring and structural condition assessment. However, research on the application of the K-means algorithm in measuring concrete structures is relatively limited, especially in the context of RC column with FRP tube. Based on the current research status, introducing the K-means algorithm and optimizing its color classification capability, as well as extending its recognition functionality for dynamic RC column with FRP tube, is expected to have a positive impact on the visual measurement of axial displacement and deformation in concrete structural axial compression tests.

Image semantic segmentation is an emerging image processing technique in image processing and represents a fundamental yet challenging tasks in the field of computer vision [31]. Over recent years, significant progress has been made in this area, particularly in medical image analysis, where it has made substantial contributions to the field of biomedical imaging. Although its application within the structural domain remains somewhat limited, it has a great potential in non-contact structural monitoring and structural condition assessment due to its excellent segmentation capabilities. U-Net model, one of the popular models in image semantic segmentation, has garnered attention for its effectiveness in various applications [32]. A notable instance of its application is in deformation analysis, where Dai et al. have effectively used an enhanced U-Net model to extract time-series information on landslide deformation from remote sensing data [33]. These successful implementations highlight U-Net's potential in measuring deformation in of RC columns. By employing the U-Net model, calibrated samples can be utilized to achieve dynamic segmentation, recognition, and measurement of RC column with FRP tubes. This approach facilitates non-contact visual dynamic tracking and measurement in structural testing, providing valuable insights into the behavior and performance of these structures. Based on the current research status, the integration of the U-Net model offers promising prospects for advancing non-contact image-based structural analysis and monitoring.

The primary contributions of this work consists of four main areas. (1) The feasibility of using semantic segmentation (U-Net) and cluster segmentation (K-means, specifically for the extraction of visual deformation in engineering column applications, have been investigated. The two segmentation approaches are integrated with classic digital image processing techniques for extracting deformation. (2) In semantic segmentation, feature extraction has been optimized through the expansion of the sensory field. As for clustering segmentation, the elbow method has been utilized for determining the optimal partition, and time series features have been introduced to improve the K-means method for improved target recognition. (3) The paper proposes an anomalous frame rejection technique for solving visual occlusion due to frame skipping problem and unintended personnel presence issue in camera captured videos. (4) Finally, the experimental environment of this study, being complex and ever-changing, has been instrumental in increasing the robustness of image processing systems. This not only aids in addressing specific problems but also contributes to advancing further research and applications in this domain.

Significantly, there is a notable research gap in deformation measurement without background processing and surface texture enhancement, particularly in complex environments. The main objective of this study is to addresses this gap, providing significant advancements and insights. Building upon previous research, this paper incorporates image enhancement in pre-processing, achieving comprehensive object integrity in deformation monitoring and measurement via image segmentation. This method has shown improved accuracy upon verification.

2. Methodology

A visual deformation tracking measurement method is proposed which aims to reduce the measurement cost and complexity of the wiring time for large reinforced concrete columns. This study investigates the capability of two image segmentation methods [34] for continuous offset deformation tracking measurement of 2D images. A related image processing framework is developed by combining the characteristics of dynamic processing and offset deformation. The first image segmentation approach used in this study is a clustering-based color segmentation method for the recognition measurement of displacement deformation in RC column with FRP tubes [35]. It is used to verify the feasibility of the image segmentation visual measurement system for measurement under deformation. The second image segmentation approach involves using semantic segmentation to visually track and measure the offset deformation of RC column with FRP tubes in axial compression experiments, and to collect images of offset deformation.

In order to provide a comprehensive overview of the image processing methods employed in capturing for full-field deformation of RC

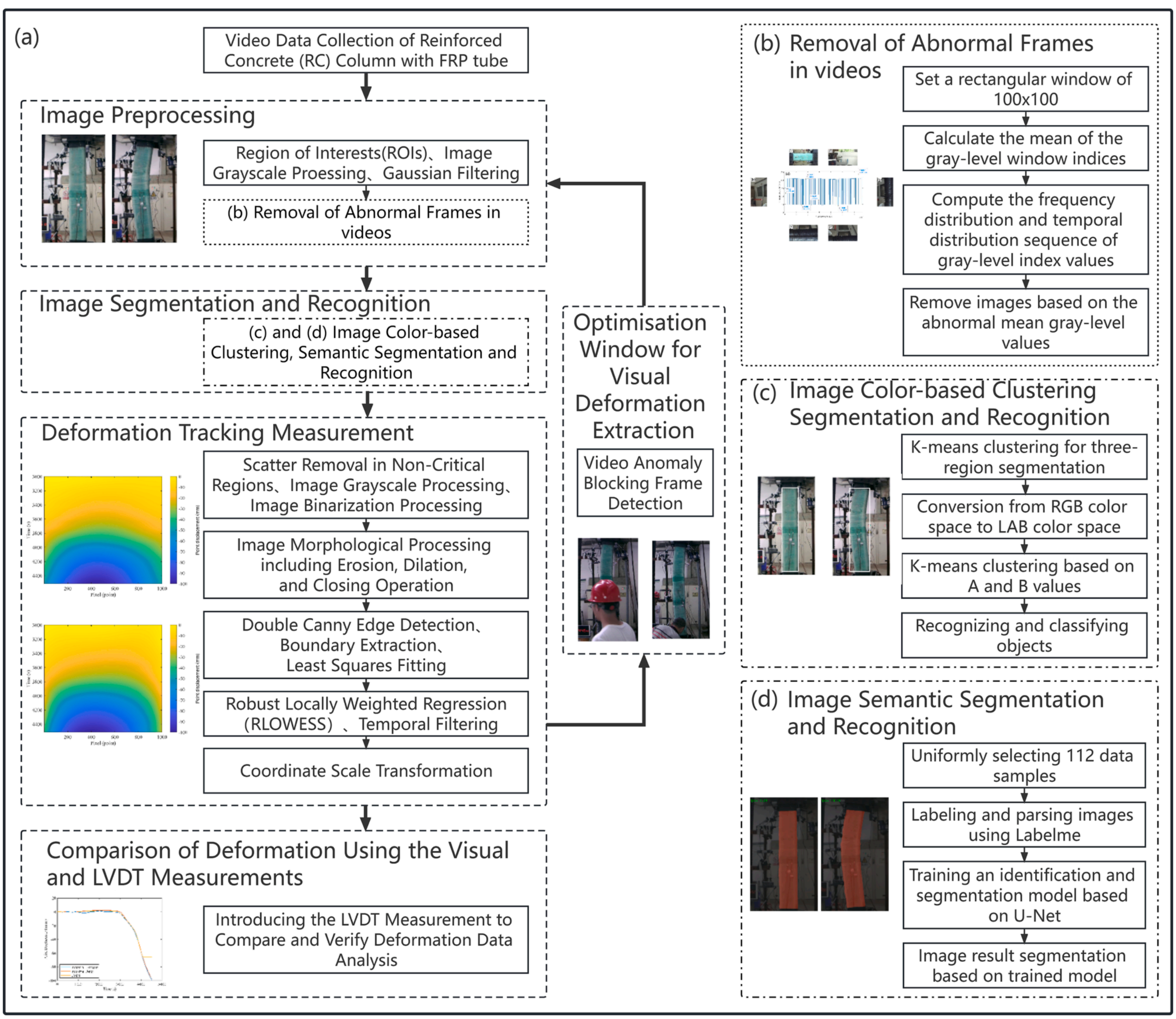

Fig. 1. (a) Measuring displacement using image segmentation; (b) Removal of abnormal framers in images; (c) Image color-based clustering segmentation and recognition; (d) Image semantic segmentation and recognition.

column with FRP tubes within complex dynamic environments, the complete processing workflow of the image recognition and measurement for the RC column with FRP tubes are shown in Fig. 1. The overall design of the visual system mainly consists of five components: image pre-processing, image segmentation and recognition, deformation tracking and measurement, system optimization window, and comparison and verification analysis of visual and displacement measurement results. The main process corresponding to these components can be summarized as follows:

(1) Image and video data are collected using a regular industrial camera. Abnormal frames are detected and processed using image pre-processing methods;
(2) Clustering image segmentation and semantic image segmentation principles are employed to optimize and enhance the recognition, tracking, and segmentation of the deformation in RC column with FRP tube before and after deformation occur;
(3) Deformation tracking algorithms are applied to analyze the tracking, measurement, and deformation of RC column with FRP tubes;
(4) Measurement results are optimized through a system optimization window to enhance measurement accuracy. The optimization focuses on rectifying abnormal frame results caused by issues such as video frame skipping, personnel obstruction, and displacement measurement failures;
(5) The accuracy and stability of the visual system's measurement results are evaluated by comparing and analyzing them with the results obtained from the LVDT. The comparative analysis can help in determining the applicable range and performance of the visual system, facilitating further optimization of the system design and implementation.

2.1. Image processing algorithms

This work presents the development of image processing algorithms using MATLAB programming language and the PyCharm integrated development environment. It enables automatic tracking [36], recognition [37], segmentation [38], and measurement of visual deformation in concrete columns with FRP tubes, and calculates related deformation quantities.

Because the extensive time span and complex environmental conditions of the dynamic experiment of RC column with FRP tubes, conventional image processing algorithms alone are insufficient for conducting deformation analysis. Therefore, algorithm enhancement and image pre-processing techniques are needed to adapt the experimental samples. Throughout the processing stage, data images suitable for image segmentation and recognition are obtained by performing grayscale conversion, Gaussian filtering [39], and abnormal frame removal on the images.

Grayscale conversion is the process of converting a color image to a grayscale image. In the grayscale conversion process, the RGB values of each pixel are converted into a single grayscale value, which represents the brightness of the pixel. The formula for the weighted average algorithm of the grayscale value is as follows [40]:

$$Gray(x,y) = 0.299 \times R(x,y) + 0.587 \times G(x,y) + 0.114 \times B(x,y) \tag{1}$$

Where R, G, and B represent the values of the red, green, and blue channels in a color image, and Gray represents the resulting grayscale value; x and y represent the coordinates of a pixel.

During the experiment, Gaussian filtering is then applied to mitigate the presence of Gaussian noise in the images. This process helps in the extraction of window features from the images, facilitating the subsequent removal of abnormal frames with greater ease. The function for Gaussian filtering is as follows [41]:

$$G(x,y) = \frac{1}{2\pi\delta^2} exp(-\frac{x^2+y^2}{2\delta^2}) \tag{2}$$

Where x and y represent the horizontal and vertical coordinates of the pixel, σ represents the standard deviation of the Gaussian distribution, and $G(x, y)$ represents the Gaussian value at the coordinate (x, y). In Gaussian filtering, a 3x3 convolution kernel is typically used for smaller smoothing operations, while a 7x7 convolution kernel is larger and leads to stronger smoothing effects. A 5x5 convolution kernel can better handle variations in lighting conditions while maintaining moderate smoothing, reducing the problem of anomalies and missing boundaries. The convolution kernel of the 5 × 5 Gaussian filter [42] used in this study is shown below [43]:

$$Core = \begin{bmatrix} 0.0030 & 0.0133 & 0.0219 & 0.0133 & 0.0030 \\ 0.0133 & 0.0596 & 0.0983 & 0.0596 & 0.0133 \\ 0.0219 & 0.0983 & 0.1621 & 0.0983 & 0.0219 \\ 0.0133 & 0.0596 & 0.0983 & 0.0596 & 0.0133 \\ 0.0030 & 0.0133 & 0.0219 & 0.0133 & 0.0030 \end{bmatrix} \tag{3}$$

Subsequently, the abnormal frame removal process is executed to minimize measurement errors in dynamic imaging. Initially, the image abnormal frame removal technique was developed to address the problem of frame skipping issues arising from camera movement during image and video capture in the experimental environment [44,45]. Later on, this technique was also employed in measurement processes to overcome obstructions caused by experimenters passing in front of the camera while correcting cylinders and sensors, which could lead to anomalies in the captured images [46,47]. Through image segmentation and frequency analysis, abnormal frames are identified and subsequently eliminated using this technique. As a result, image quality [48] and measurement accuracy can be improved. In related studies anomaly removal and defocus increase in images are effective methods to resolve anomalous states.

The image abnormal frame removal technique is mainly focuses on setting the measurement object window for filtered images. The window size is usually set to 100 × 100, although it can also be adjusted based on the image and target size. The average grayscale value is calculated within the window and frequency statistics are performed. Then, based on the statistical analysis of abnormal grayscale values, outliers are removed to improve both image quality and measurement accuracy. The function for calculating the average gray value within the window is as follows [49,50]:

$$P = \frac{\sum_1^{\Delta x}\sum_1^{\Delta y} Gray(x,y)}{\Delta x \times \Delta y} \tag{4}$$

Where P represents the gray window value of 100 × 100, Δx and Δy represent the pixel size of the window setting.

Experiments were conducted to examine the characteristics of the abnormal frames. The analysis revealed that gray values of the abnormal frame mainly falling within the range above 200 and below 220, as shown in Fig. 2(a). Fig. 2(b) illustrates the time series statistics of the mean grayscale values within the window, which serve as a basis for identifying abnormal frames. The frequency distribution histogram and temporal Gaussian grayscale mean sequence of the repair results obtained through the utilization of abnormal frame repair methods are presented in Fig. 2(c) and Fig. 2(d), respectively. Fig. 3 illustrates the video abnormal frames removed by the time series of mean gray values within the window and the correlation of the image [51].

2.2. Image segmentation and recognition

Two image segmentation methods are implemented to solve the segmentation and recognition problem of RC column with FRP tubes, namely image color-based clustering segmentation recognition and semantic segmentation recognition.

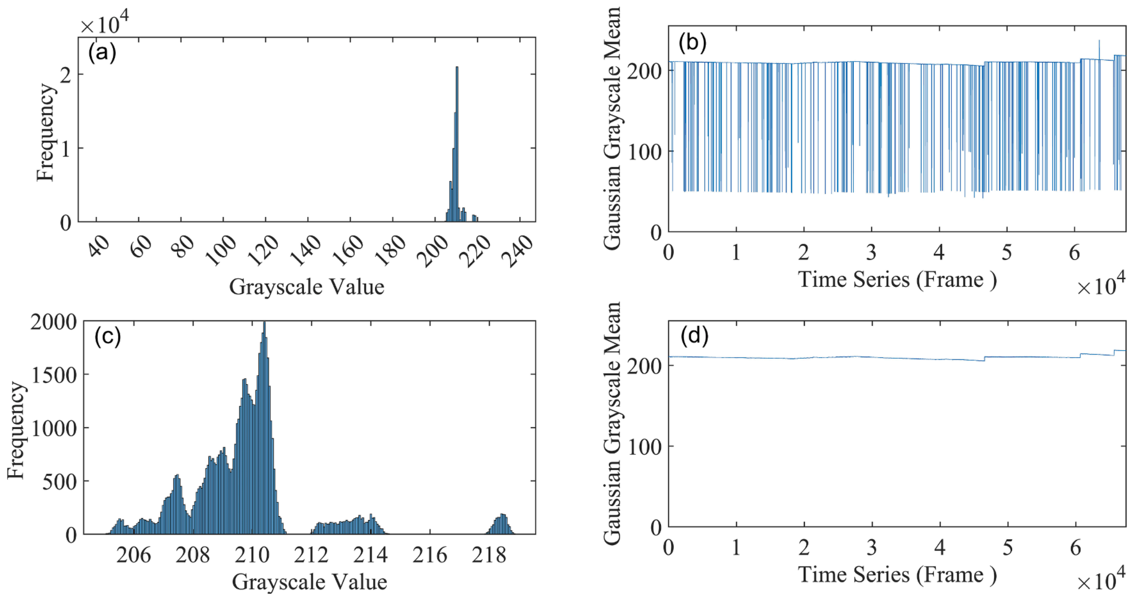

Fig. 2. Experiment 0412. (a) Frequency distribution histogram of the grayscale window for images with abnormal frames; (b) Time series of grayscale windows for images with abnormal frames; (c) Frequency distribution histogram of the grayscale window after removing images with abnormal frames; (d) Time series of grayscale windows after removing images with abnormal frames.

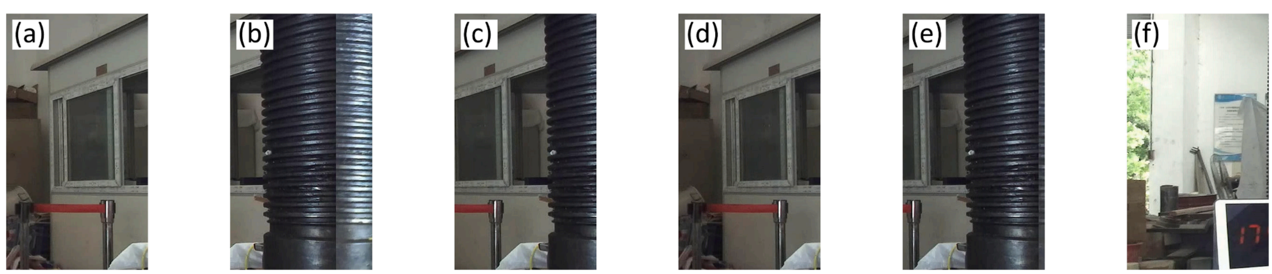

Fig. 3. (a) Frame 982 video image; (b) Frame 14,544 video image; (c) Frame 29,447 video image; (d) Frame 35,538 video image; (e) Frame 46,426 video image; (f) Frame 63,649 video image.

2.2.1. *Image color-based clustering segmentation and recognition*

In the image clustering segmentation recognition, the process involves four steps [52,53]:

(1) Conversion of the RGB color model of the image into the LAB color model;
(2) Extraction of the B value matrix of the image, followed by the application of the elbow method to determine the optimal K value for clustering segmentation;
(3) Utilization of the K-means algorithm for iterative classification of the A and B values in the LAB model;
(4) Confirmation and recognition of the object detection using moving window.

Compared to the XYZ model of RGB [54], the LAB model [55] is more favored in color clustering and segmentation tasks, mainly because of its better perceptual consistency, device independence, and accuracy of color difference calculation [55,56]. It better reflects human perception of color and provides a more stable and reliable representation of color; When performing color model conversion, the RGB image is converted to the XYZ color space to compensate for the shortcomings of the RGB model. Equation (5) is used for color space conversion, and the function is as follows [57]:

$$\begin{bmatrix} X \\ Y \\ Z \end{bmatrix} = A \begin{bmatrix} R \\ G \\ B \end{bmatrix} = \begin{bmatrix} a_{11} & a_{12} & a_{13} \\ a_{21} & a_{22} & a_{23} \\ a_{31} & a_{32} & a_{33} \end{bmatrix} \begin{bmatrix} R \\ G \\ B \end{bmatrix} \tag{5}$$

where R, G, and B represent the channel matrices of the captured image, A represents the color channel coefficient matrix, and X, Y, and Z represent the spatial coordinates of the image.

Once the B channel is obtained, the optimal value of K for clustering segmentation (i.e. the number of clusters) can be determined using the elbow method. The elbow method [58] utilizes the color features of the target object with a specific focus on the B value. The function for elbow method is as follows:

$$SSE = \sum_{i=1}^{k} \sum_{p \in C_i} |p - m_i|^2 \tag{6}$$

here, C_i represents the i-th cluster, p is all the sample points in that cluster, and m_i is the centroid of the cluster (i.e., the mean of all the samples in the cluster).

The result of determining the optimal K value using the elbow method is shown in Fig. 4. The graph, derived from 112 images uniformly sampled from the video stream, shows the relationship between the K value and the average sum of squared errors. This relationship allows to determine the optimal number of clusters. According to the observation from graph, it is determined that the optimal K value is 3.

Once the number of clusters is determined, the K-means clustering method is applied for classification. The typical steps involved in K-

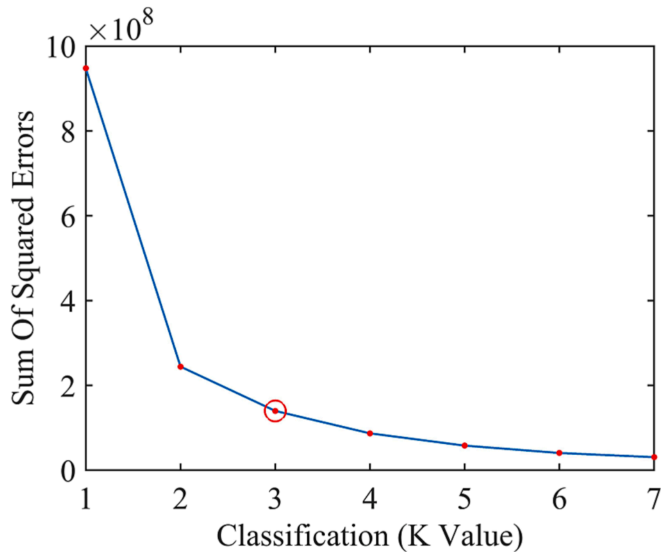

Fig. 4. Elbow method plot of clustering deviation with different K values.

means clustering are as following [59,60]:

(1) Initialization: Each observation is considered as a separate cluster.
(2) Distance calculation: The distance between each cluster is calculated, typically using Euclidean or Manhattan distance.
(3) Cluster merging: The two closest clusters are merged into a new cluster, and the distance between the new cluster and other clusters is recalculated.
(4) Repeat steps 2 and 3 until a certain convergence criterion is met. This criterion can be defined as the number of clusters no longer changing or the distance moved by the cluster centers being less than a predefined threshold. The final result is a set of clusters, each containing a set of similar observations.

Although K-means clustering has proven effective for image segmentation, it falls short in recognizing target objects. To address this limitation, the approach is enhanced by utilizing Equation (4) to compute the gray window values on each classified image, specifically for cavity detection. The maximum calculated value is considered as the target recognition object. Subsequently, a reclassification sorting process is performed to select the matrix set of images containing the target objects, thereby completing the identification of target objects within image clustering. The segmentation [61] and recognition outcomes for RC column with FRP tube are shown in Fig. 5.

2.2.2. *Image semantic segmentation and recognition*

Semantic segmentation refers to the process of assigning each element in an image to a predefined semantic category, which is different from image clustering segmentation. U-Net, is a convolutional neural network-based image segmentation model proposed by Ronneberger et al. in 2015. It has been widely used in medical image segmentation tasks, especially in tasks that require high accuracy for small structures, and has shown excellent performance [25].

The structure of U-Net consists of symmetric encoder and decoder components. The encoder part includes convolutional layers and max pooling layers, which are used to extract image features and gradually reduce the image size. The decoder part includes convolutional layers and up-sampling layers, which are used to gradually restore the shrunken feature maps to the original image size and perform pixel-level classification. In the decoder, each layer concatenates the feature map from the previous layer with the corresponding output from the encoder, in order to preserve more spatial information. The U-net network is composed of five effective feature layers with a training depth of 5. The size of the convolution kernel for the U-shaped structure is 3x3. Across these feature layers, both the number and value of the convolution kernels vary. Initially, the number of convolutional kernels is 64, which is gradually scaled up by a factor of 2 until it reaches 512 through 2x2 maximum pooling as the depth increases [62].

In this study, a semantic segmentation method for RC column with FRP tube is designed and validated using the U-Net architecture [63]. The method consists of four steps: (1) uniformly selecting 112 data samples; (2) annotating images using the LABELME tool [64] and batch parsing the annotation information through scripts; (3) training the U-Net segmentation model using the parsed annotation information; and (4) using the trained model for semantic segmentation and prediction of the overall experimental data.

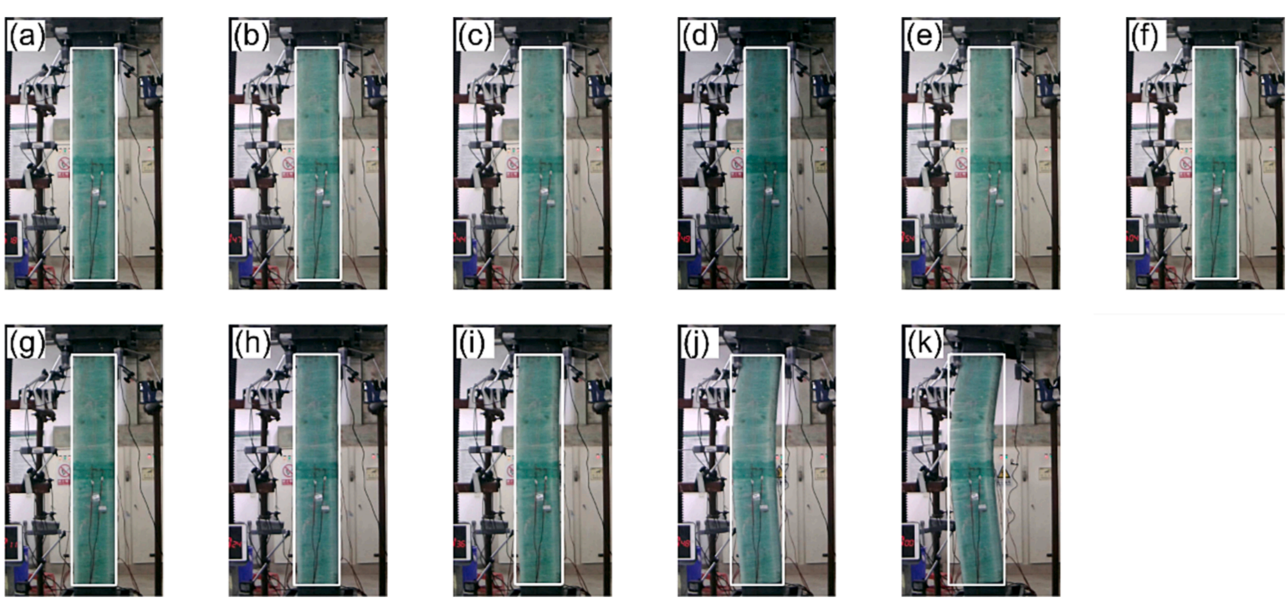

Fig. 5. The clustering-based image segmentation and recognition results of experiment 0412. (a) Frame 1240 video image; (b) Frame 6090 video image; (c) Frame 11,425 video image; (d) Frame 16,760 video image; (e) Frame 22,095 video image; (f) Frame 27,430 video image; (g) Frame 32,765 video image; (h) Frame 38,100 video image; (i) Frame 43,435 video image; (j) Frame 48,770 video image; (k) Frame 54,105 video image.

In this study, a total of 54,180 frames (i.e. image samples for experiment 0412) were captured using an industrial camera, operating at an actual frame rate of 12.42 FPS. For the purpose of training, an average of 500 frames were selected for annotation and parsing for training. The annotation information was parsed into original images (a), bottom images (b), and annotated images (c) using scripts, as shown in Fig. 6.

The segmentation recognition results achieved through the use of U-Net semantic segmentation method is shown in Fig. 7.

2.3. Deformation tracking measurement

The visual deformation tracking measurement in this work consists of five parts, which are:

1) Non-key area scatter point cleaning, image grayscale and binarization;
2) Image morphology processing [65], including erosion, dilation, and closing operations;
3) Canny bilateral edge processing [66], boundary line extraction, and fourth-order polynomial least squares fitting;
4) Robust locally weighted regression (RLOWESS) [67] and time filtering [68];
5) Coordinate scale transformation.

This method uses the results of segmented images, first to clean non-key area points (only in the case of image clustering segmentation) and operate within the recognition box of cluster segmentation as boundaries. The function for grayscale conversion of the image is shown in equation (4), and the function for image binarization is as follows [69]:

$$B(x,y)=\begin{cases}1 if G(x,y)\geq T,\\ 0 otherwise.\end{cases} \tag{7}$$

where B(x, y) is the binary pixel value at coordinate (x, y), which takes on a value of either 0 or 1; G(x, y) is the grayscale pixel value at that coordinate; and T is the threshold value obtained using the OTSU algorithm.

Once the binary images are generated, image morphology processing methods are employed [70]. Firstly, the erosion operation is applied to eliminate the noise on the edge of the RC column with FRP tube, reduce the size of the target, and remove the scattered spots within the erosion area to make the edge clearer. Then, the dilation operation is used to expand the shrunken area and fill in some of the target holes. Finally, the closed operation is performed for fine-tuning and filling closed regions. This further enhances the clarity of the target edges, thereby facilitating more effective edge detection [71].

In order to obtain the edge connection lines of the segmentation result, the Canny edge detection algorithm [72] is first applied to the image that has undergone morphological processing. Then, another Canny algorithm detection is applied to the processed result to obtain the points of the inner and outer edges. The boundary extraction through truncation is crucial for displacement measurement. With more boundary area points available, curve fitting can be performed more conveniently and accurately. Finally, a fourth-order polynomial [73] is used for least-squares fitting to extract the boundary. Depending on the deformation characteristics of the column, higher and lower order polynomial fits introduce overfitting and underfitting problems, and the fourth order is an equilibrium position for the deformation characteristics. This function is represented by equation (8):

$$p=p_1x^4+p_2x^3+p_3x^2+p_4x+p_5 \tag{8}$$

Due to the large number of total frames (54180) and high frame rate (12.42 FPS) in the sample, it is challenging for the traditional method that reply on the LVDT to extract strain data. The traditional method cannot keep up with the processing speed required to handle such a large volume of data in a timely manner. To maintain the extraction of one deformation data per second (compared to the LVDT rate of one deformation data every three seconds), an enhanced frame is extracted from every three frames and, subsequently, temporal filtering is applied to obtain a single result value for every four enhanced frames [74]. The reason for using RLOWESS for the optimization process is because its local linear regression characteristics are more in line with the trend of the column deformation, and it has shown the best optimization performance after the comparison carried out by a number of optimization methods, such as moving, lowess, loess, sgolay, and rloess.

Finally, a scale transformation method is applied to obtain the actual deformation and displacement. This method is based on the conversion relationship between the lateral average of the initial n (n = 10) frames segmentation results and the width of the RC column with FRP tubes, which is 210 mm [75]. By using this method, accurate measurement parameters can be obtained without camera calibration. The scale transformation function is shown in equation (9):

$$S=\frac{210\times n}{\sum_{i=1}^{n}\frac{\sum_{j=1}^{m}(x_2-x_1)}{m}} \tag{9}$$

where x represents the horizontal axis of the cylinder in the picture, x_1 is the coordinate of the left border pixel, x_2 is the coordinate of the right border pixel, m represents the number of pixels on the vertical axis of the cylinder, and n is the frame number of the picture.

2.4. Optimization window for deformation visual measurement

The main purpose of the extraction of the system optimization window is to mitigate the impact of abnormal video data captured during experiments. This issue arises due to the open nature of the experimental site, which may lead to visual measurement errors caused by non-relevant personnel entering the area. By implementing the system optimization window, such errors can be identified and rectified, leading to improved accuracy and reliability in the visual measurements. To tackle this issue [37], the system is optimized by using the image abnormal frame removal technique (Section 2.1), the statistical results are shown in Fig. 8. Through the histogram of the frequency distribution of the Gaussian gray mean value in Fig. 8 (a) and the time series of the window average gray value in Fig. 8 (b); Statistics show that a single abnormal frame removal technology cannot meet the instability and uncertainty problems of personnel occlusion. Therefore, based on the results of image visual segmentation [76], multiple times of removing abnormal frames are proposed to solve this problem. The histogram of the processing results is shown in Fig. 8 (c), and the time series diagram of the gray value is shown in Fig. 8 (d). The time series of silhouette frame rejection in Fig. 8 is based on the same principle as in Fig. 2. The main purpose of the iteration process is to address the problem of frames with insignificant differentiation. A close examination of Fig. 8 (a) reveals that the abnormal frames are predominantly clustered around the value 0. Through the iterative process, this method refines the assessment of frame abnormality by progressively narrowing

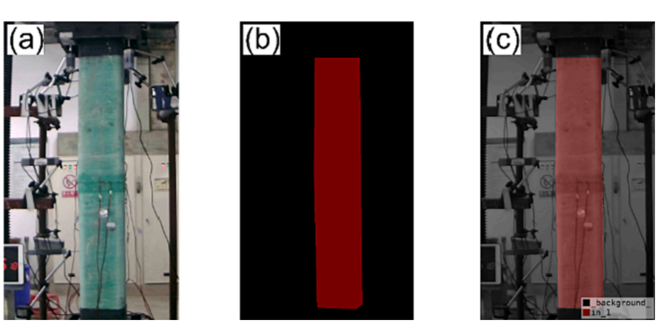

Fig. 6. (a) Original image; (b) Bottom image; (c) Annotate image.

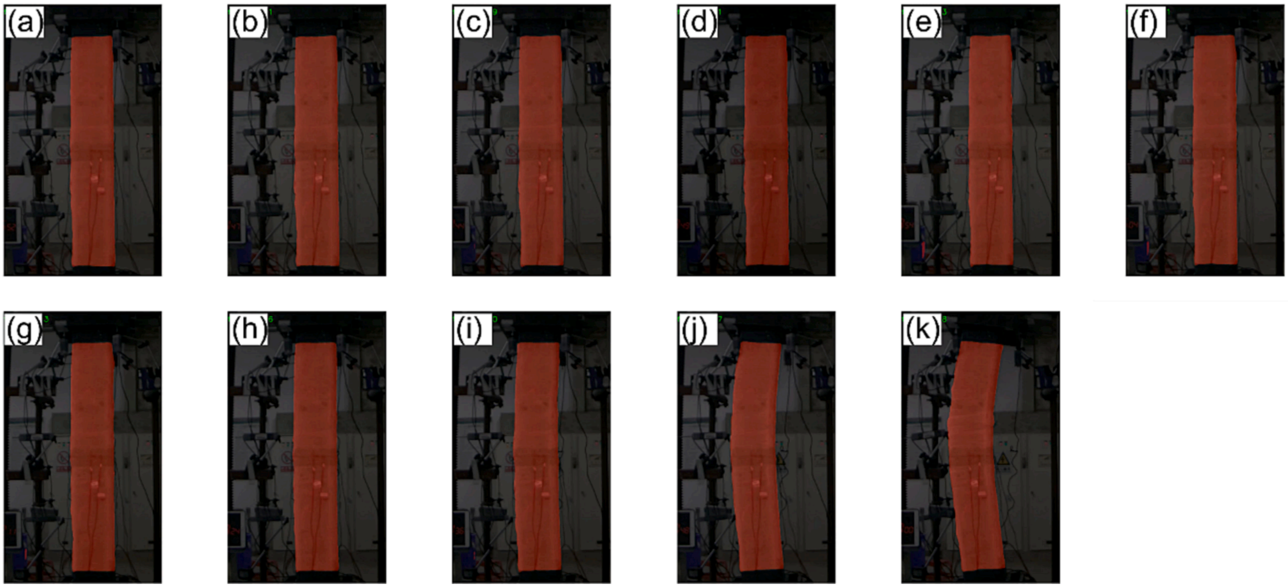

Fig. 7. The semantic image segmentation and recognition results of experiment 0412. (a) Frame 1240 video image; (b) Frame 6090 video image; (c) Frame 11,425 video image; (d) Frame 16,760 video image; (e) Frame 22,095 video image; (f) Frame 27,430 video image; (g) Frame 32,765 video image; (h) Frame 38,100 video image; (i) Frame 43,435 video image; (j) Frame 48,770 video image; (k) Frame 54,105 video image.

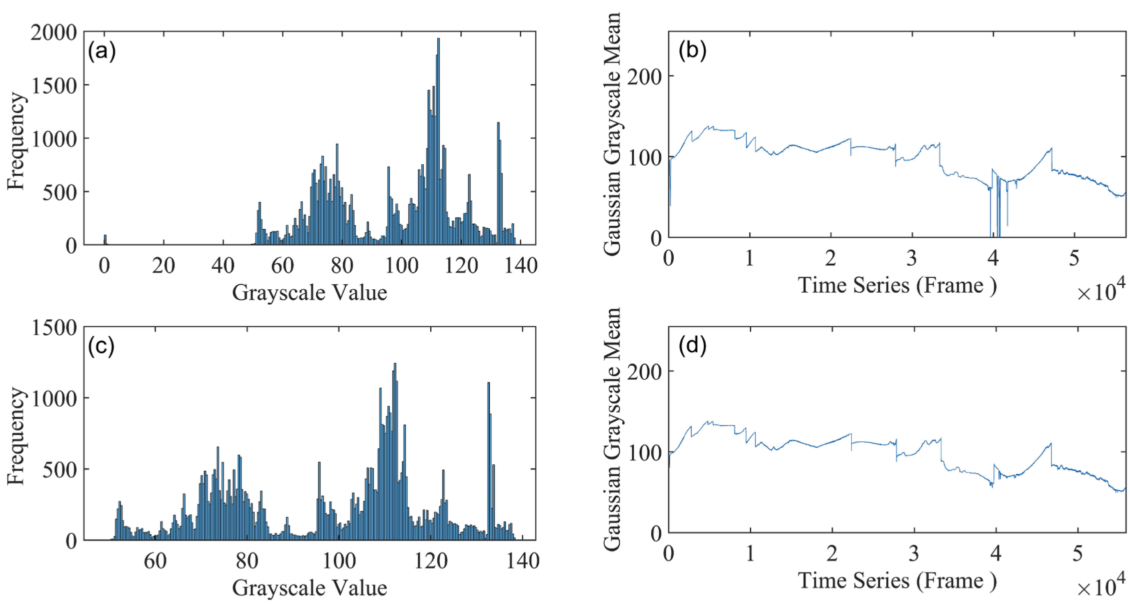

Fig. 8. Experiment 0413. (a) Frequency distribution histogram of the grayscale window for images with personnel occlusion; (b) Time series of grayscale windows for images with personnel occlusion; (c) Frequency distribution histogram of grayscale windows for images with personnel occlusion after removing occlusion; (d) Time series of grayscale windows for images with personnel occlusion after removing occlusion.

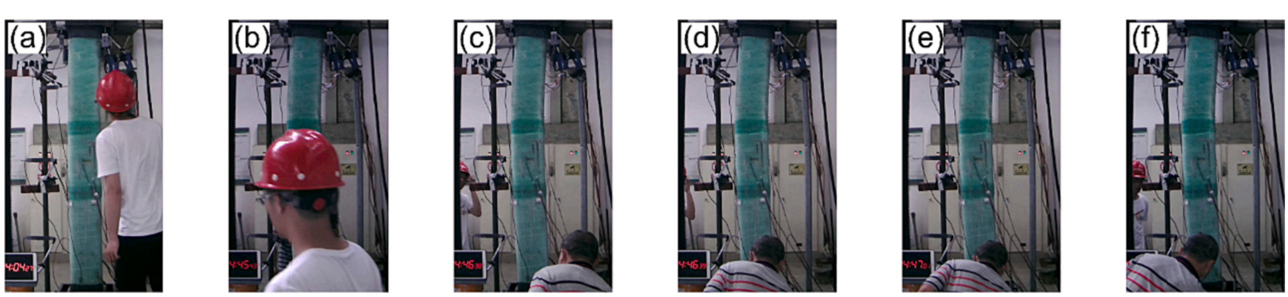

Fig. 9. (a) Frame 217 video image; (b) Frame 39,644 video image; (c) Frame 40,468 video image; (d) Frame 40,486 video image; (e) Frame 40,818 video image; (f) Frame 41,741 video image.

the analysis window. A total of 257 frames of video abnormal frames were eliminated through multiple iterations, an example is shown in Fig. 9. This optimization step enhances the accuracy and reliability of the system by eliminating visual measurement errors caused by irrelevant personnel or other disturbances within the experimental area.

2.5. Comparison and verification analysis of deformation measurement using visual and displacement measurement

In a comparative and validation analysis of visual and the LVDT measurements of deformation, a method is utilized that involved extracting time-displacement curves from the global displacements. This approach enabled an assessment of the consistency and accuracy of the visual measurements by comparing them with the more traditional the LVDT measurements [77]. The visual measurements were taken at a frequency of one observation per second, while the traditional method used a frequency of one observation every three seconds with LVDT. By analyzing the time displacement curves, insights into the agreement between the two measurement methods were gained, and evaluated the overall performance of the visual system in capturing and quantifying deformations [78].

3. Experimental procedures and measurement results

The experimental equipment, related plans, and experimental results of image segmentation measurement are discussed in this section.

3.1. Experimental devices

The experimental setup consists of three parts: (1) Axial compression machine operation equipment, RC Column with FRP tubes, and other related experimental equipment; (2) Traditional displacement sensor-based strain measurement system, including displacement sensors, data acquisition cables, data acquisition instruments, and a laptop; (3) Vision-based deformation measurement system, consisting of an industrial camera, a camera mount, two laptops, and a laser rangefinder.

The software and hardware platform of the established visual segmentation and recognition measurement system has been applied in the axial compression experiment of RC Column with FRP tubes, aiming to measure the overall deformation and failure mode of the RC column with FRP tube during axial compression. The experimental setup shown in Fig. 10. Among them, the resolution of ordinary industrial cameras in Fig. 10 (d) is 1920 × 1080, and the frame rate is 30 FPS.

3.2. Experimental design

In the experiments of compressive and tensile testing of RC column with FRP tube specimens (the term FRP experiment is used from here on), a constant axial load N is applied to the specimens, and the horizontal displacement is measured using a displacement transducer (item (c) in Fig. 10), employing a contact-based measurement method. The specifications of the LVDT are in accordance with the relevant standard. The experiments are conducted on a compression testing machine, where the load is gradually increased to 2800 KN and then gradually unloaded over time.

The experimental design in this work centers around the utilization of the visual deformation measurement system for accurate deformation and displacement measurements. The visual segmentation recognition measurement system consists of several components: (1) an ordinary industrial camera (resolution 1920 × 1080) and a ZED camera (resolution 1920 × 1080), supported by a tripod with built-in level; (2) two laptops (HP ENVY15 X13 i5 and Mate-Book D 2018 i7), are utilized for data acquisition; (3) a laser rangefinder is employed for distance measurement.

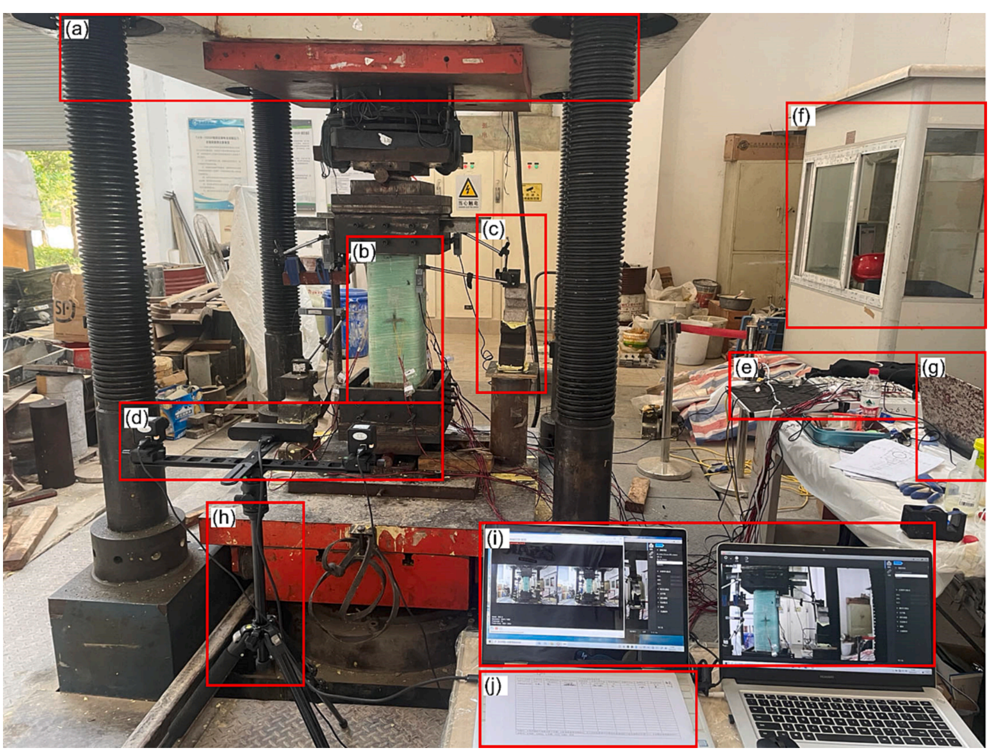

Fig. 10. Structural Design of Experimental Devices; Item (a): Axial compression machine; Item (b): RC column with FRP tube with dimensions of 1200 × 210 × 210 ± 5 mm, 1600 × 210 × 210 ± 5 mm, and 2000 × 210 × 210 ± 5 mm; Item (c): The LVDT sensors and their brackets; Item (d): ZED 2i camera with resolutions of 1920 × 1080 (in the middle) and ordinary industrial cameras with resolutions of 1920 × 1080 (at the two sides); Item (e): Sensor data acquisition instrument; Item (f): Control room for the compression machine; Item (g): Notebook for sensor data acquisition; Item (h): Tripod for camera fixation; Item (i): data acquisition notebooks HP ENVY15 X13 i5 (on the left), and Mate-Book D 2018 i7 (on the right); Item (j): Experimental record sheet.

The main purpose of this experiment conducted here is to evaluate the capability of the visual deformation measurement system in accurately quantifying deformations and displacements with in the RC column with FRP tube experiment. The FRP experiments are conducted nine times, using specimens of different sizes, to assess the performance of the proposed visual deformation measurement system. Table 1 illustrates the measurement setup information, specifically related to the visual shooting distance and shooting height, which vary in relation to the height of the concrete column.

3.3. Experimental results and analysis

3.3.1. Displacement and deformation measurement

The displacement measurements (without applying RLOWESS) derived along the edge of the RC column with FRP tubes are shown in Fig. 11. It is worth to note that the negative displacement value indicates the deformation moving towards west, and vice versa. Fig. 11(a) shows the measurement result obtained by image color-based clustering segmentation (K-means) where Fig. 11(b) shows the measurement result derived by image semantic segmentation (U-Net). The deformation information is derived based on the 2D statistical analysis of deformation data, as described in steps 1–3 of Section 2.3. The core information conveyed in Fig. 11 includes three aspects: Time (in seconds), Pixel (point), and Displacement (mm). The axes in the figure are structured with time and point, where the time is plotted on the x-axis and point on the y-axis. The displacements, with their directions, are indicated by the colors within the figure. Specifically, the y-axis represents the variation in displacement of a pixel over time, whereas the x-axis shows the displacement changes of pixels at a specific time.

As can be seen in Fig. 11, some abnormal fluctuating values have been observed, which are likely the caused by the undetected abnormal frames. To address the issue of abrupt displacement changes, the RLOWESS method has been applied to optimize the measurement. A great improvement in the measurement stability has been observed after applying the RLOWESS method, which can be seen in Fig. 12.

For example, in Fig. 11, the red solid line (LVDT), the black dotted line (200th point), and the red dotted line (800th point) are compared before and after partial optimization. Its stability has been greatly improved, as shown in Fig. 12.

The optimized displacement measurements (after applying RLOWESS) derived along the edge of the RC column with FRP tubes are shown in Fig. 13. It can be seen that issue of the abnormal fluctuating values have been addressed. In generally, improvement in measurement stability has been observed in both cameras (industrial camera and ZED camera) for almost all 9 experiments after applying RLOWESS (see Appendix S1 for the experimental results from the rest of the groups and cameras).

The LVDT point represents a unified point between the visual measurement point and the sensor LVDT measurement point. Verification and analyzes the results of two visual deformation measurement methods using the red solid line in Fig. 13 by comparing them with the LVDT. Fig. 14 shows the comparison of the results of experiment 0412 for the two vision methods and the LVDT.

Table 1
The overview of the specifications (i.e. The Size, Distance, and Height Distribution of RC column with FRP tubes) for the 9 experiments conducted.

Number	Size (mm)	Distance (mm)	Height (mm)
0406	1200 × 210 × 210	1997	1155
0407	1200 × 210 × 210	2002	1148
0408	1200 × 210 × 210	2002	1146
0409	1200 × 210 × 210	2000	1148
0410	1200 × 210 × 210	2003	1149
0411	1200 × 210 × 210	2002	1138
0412	1600 × 210 × 210	2500	1327
0413	2000 × 210 × 210	3219	1548
0414	2000 × 210 × 210	3290	1430

Based on the results obtained, it can be inferred that the visual deformation measurement methods show great potential to supplement the conventional deformation measurement techniques, which rely on the LVDT. Moreover, the visual measurement methods demonstrate their effectiveness even in cases when the physical measurement technique (LVDT) encounters failure. In such case, the visual measurement methods can still provide accurate single-point deformation measurement and visual-based global displacement measurement solutions.

3.3.2. Multiple experimental validation

The deformation tracking experiments on nine groups of RC column with FRP tube, using image clustering color segmentation and image semantic segmentation methods, are validated. In the experiments conducted, a comparison was made between the LVDT measurement method and the two image segmentation techniques (Table 2). The experiments from the three different target height group, namely the 0410, 0412 and 0414, are selected for further analysis. Detailed results from the other six experiments can be found in Appendix S1.

For the case of experiment 0412, the maximum deviation observed for the K-means image segmentation is 2.36 mm, while the maximum deviation of the image semantic segmentation recognition is 1.45 mm. These deviations were observed in the context of a maximum deformation value of 100 mm. Furthermore, the maximum standard deviation of average deformation offset for the K-means image segmentation measurement method is 0.66 mm, and for the image semantic segmentation recognition measurement method is 0.34 mm. These standard deviations indicate the level of variability in the measurement results. The average relative measurement error for the K-means image segmentation measurement method is found to be 1.1 %, and for the image semantic segmentation recognition measurement method is 0.4 %. Due to the incompleteness of the LVDT measurements, the two visual methods were cross-validation for a more comprehensive comparison. The standard deviation of difference observed is 0.78 mm and the maximum deviation is 2.55 mm. This relative measurement error provides insights into the accuracy of the measurement methods compared to the ground truth provided by the LVDT method.

Based on the aforementioned visual deformation measurement method, the overall deformations of the RC column with FRP tube for the case of experiments 0410 (with a height of 1200 mm) and 0414 (with a height of 2000 mm) are shown in Fig. 15. The deformations exhibit eastward displacement, indicating positive values in the displacement direction. The comparisons with LVDT are shown in Fig. 16.

In the cases of experiments 0410 and 0414, the LVDT measurement components encountered varying degrees of failure. In the experiment 0410, the LVDT failure was relatively minor, with measurement range reaching its limit and ceasing to continue measurement only between data points 4821 and 5145. However, in the experiment 0414, the LVDT failure was more severe. The LVDT became jammed during the measurement process, resulting in the inability to obtain valid measurements between measurement points 2386 and 4558.

In the experiment 0410, comparing the data of the two visual deformation measurement methods with the LVDT in the effective time interval (1: 4821), it was found that the maximum deviations were 2.98 mm and 4.01 mm, with relative standard deviations of 1.55 mm and 1.39 mm, respectively. The cross-validation of the two visual methods shows a standard deviation difference of 2.62 mm and a maximum deviation of 6.23 mm.

For experiment 0414, the comparison with the LVDT within the effective time interval (1:2386) shows maximum deviations of 1.25 mm and 1.34 mm, with relative standard deviations of 0.54 mm and 0.49 mm, for the two methods, respectively. In the cross-validation of the two visual methods, a standard deviation of 0.73 mm and a maximum deviation of 3.04 mm are observed.

The experimental findings, particularly highlighted in Experiment

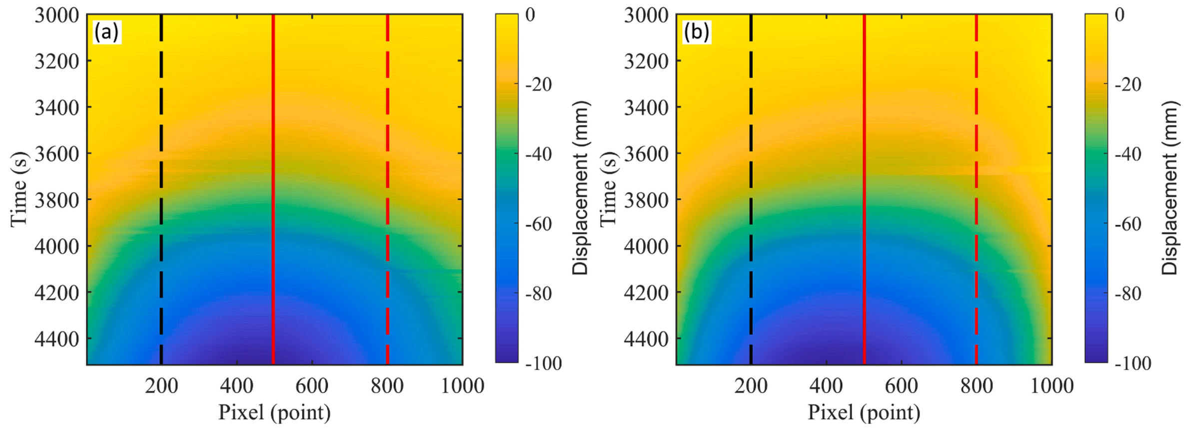

Fig. 11. Deformation measurement results (without RLOWESS) for Experiment 0412 derived from (a) K-means method; (b) U-Net method. The red solid line represents the position at the 500th (LVDT) point of the measurement, the black and red dashed lines represent the 200th and 800th point of the measurement, respectively. (For interpretation of the references to color in this figure legend, the reader is referred to the web version of this article.)

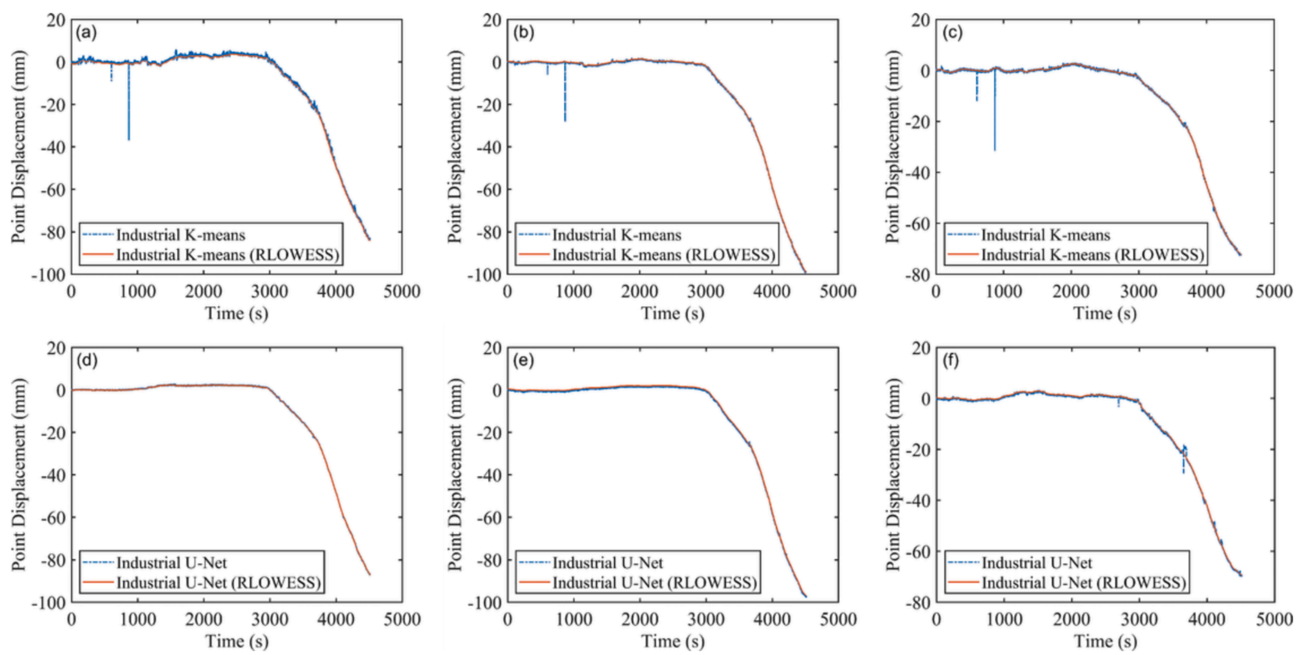

Fig. 12. The K-means derived displacement curve at the (a) 200th point (black dotted line from Fig. 11); (b) at LVDT measurement point (solid red line from Fig. 11); (c) 800th point (red dotted line from Fig. 11). The U-Net derived displacement curve at the (d) 200th point (black dotted line from Fig. 11); (e) at LVDT measurement point (solid red line from Fig. 11); (f) 800th point (red dotted line from Fig. 11). (For interpretation of the references to color in this figure legend, the reader is referred to the web version of this article.)

0412, reveal distinct observations across various deformation stages. During the initial small deformation stage (0 s-1100 s), where the deformation and displacement of the columns are within 1 mm, the measurements obtained from both visual methods and the Linear Variable Differential Transformer (LVDT) are largely consistent. However, in the medium deformation stage (1100 s-3000 s), when the deformation exceeds 1 mm and reaches the inflection point, a notable discrepancy emerges. The results from the K-means method exhibit greater deviation, whereas the U-Net method maintains more stability. This disparity could be attributed to the influence of background and lighting conditions in moderate deformations, potentially leading to compounding effects. As the experiment progresses beyond the inflection point (time above 3000 s), a substantial large deformation is observed. In this stage, the relative standard deviation of the K-means method slightly outperforms that of the U-Net method. Both visual methods effectively capture the evident changes in the column during this large deformation stage. Analyzing these deformation stages in detail is crucial for a comprehensive understanding of the applicability and limitations of the two visual methods and LVDT measurements under varying deformation conditions.

Based on the observation results from the three sets of experiments (0410, 0412, and 0414), a positive correlation between the height of the RC column with FRP tube and the deformation variables has been observed. Table 2 presents the comparison results of visual measurements and LVDT measurements in terms of relative maximum deviation, standard deviation, and relative error of the deformation within the RC column with FRP tube, expanding across 9 sets of experiments. In addition, the comparison between the measurements from the two visual methods across these nine experiments shows an average standard deviation of 1.54 mm and an average maximum deviation of 4.28 mm.

Based on the results above, the following summaries can be drawn:

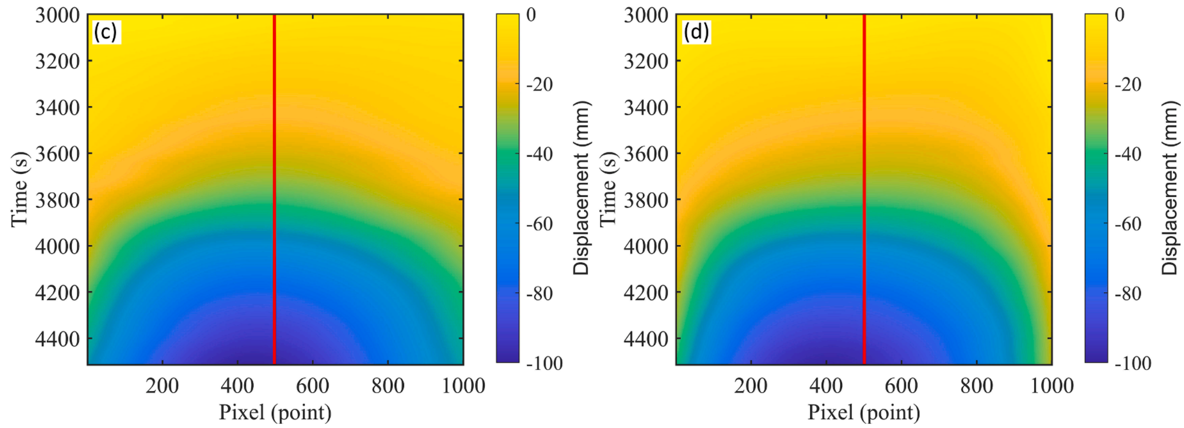

Fig. 13. (a) Deformation measurement results (after RLOWESS) for Experiment 0412 derived from (a) K-means method; (b) U-Net.

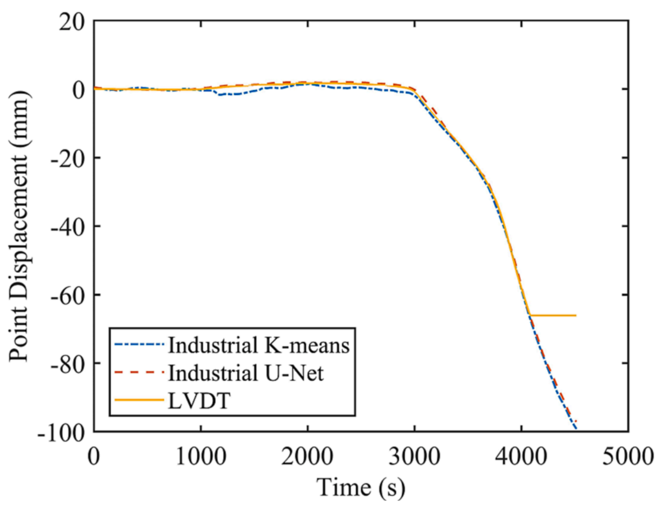

Fig. 14. Comparison between measurements derived from K-means, U-Net and LVDT for Experiment 0412.

1. The visual deformation measurement method can serve as a robust supplement to the traditional LVDT measurement, which demonstrates the potential for providing a more comprehensive deformation measurement for analysis. Moreover, the visual measurement techniques are capable of distinguishing the deformation directions, i.e. deformation towards east or vice versa.
2. Even in circumstances where traditional LVDT measurements failure due to equipment malfunctions or exceeding their measurement limits, the visual displacement measurement methods are still capable for providing consistent and reliable displacement data.
3. Based on the validation analysis of nine experiments on RC column with FRP tube, the K-means method had an average relative error of 1.03 %, while the U-Net method had an average relative error of 0.44 %. In terms of the average maximum standard deviation, the K-means method was 1.65 mm, while the U-Net method was 0.95 mm. As for the average maximum deviation, the K-means method was 4.61 mm, while the U-Net method was 3.24 mm. Thus, overall, the U-Net method performed slightly better in the deformation tracking measurements of RC columns with FRP tube axis compression tests.
4. In cases of human occlusion issues within the video, correction can be implemented using outlier frame removal techniques. However, it should be noted that the measurement accuracy maybe impacted. Despite these challenges, it is feasible to achieve the recognition of RC column with FRP tube using visual methods.

Table 2
Relative deviations between visual deformation measurement and displacement deformation measurement for the 9 experiments conducted.

Number and Method	Maximum LVDT Measurement (mm)	Visual Relative Measurement (mm)	Maximum Visual Measurement (mm)	Standard Deviation (mm)	Relative Maximum Offset (mm)	Relative Error (%)
0406 K-means	75.50	75.58	75.58	1.03	1.79	0.41
0406 U-Net	75.50	71.87	71.87	0.36	1.28	0.34
0407 K-means	87.35	86.14	86.14	1.94	3.21	0.59
0407 U-Net	87.35	88.49	88.49	0.70	2.10	0.37
0408 K-means	96.59	107.31	107.31	2.11	10.74	0.27
0408 U-Net	96.59	100.77	100.77	1.09	4.23	0.25
0409 K-means	70.87	67.31	67.31	1.77	3.96	1.88
0409 U-Net	70.87	69.28	69.28	1.42	3.64	1.13
0410 K-means	91.07	90.09	90.09	0.53	1.24	7.6e-02
0410 U-Net	91.07	87.82	87.82	0.49	1.34	2.6e-03
0411 K-means	97.81	99.71	99.71	3.10	8.59	3.18
0411 U-Net	97.81	99.13	99.13	1.02	5.21	0.29
0412 K-means	66.07	67.37	99.17	0.66	2.36	1.11
0412 U-Net	66.07	67.62	97.05	0.34	1.45	0.41
0413 K-means	67.02	62.92	93.30	2.23	6.66	1.57
0413 U-Net	67.02	64.50	91.02	1.78	5.97	0.97
0414 K-means	130.23	129.45	138.17	1.55	2.98	0.25
0414 U-Net	130.23	129.21	135.10	1.39	4.01	0.27

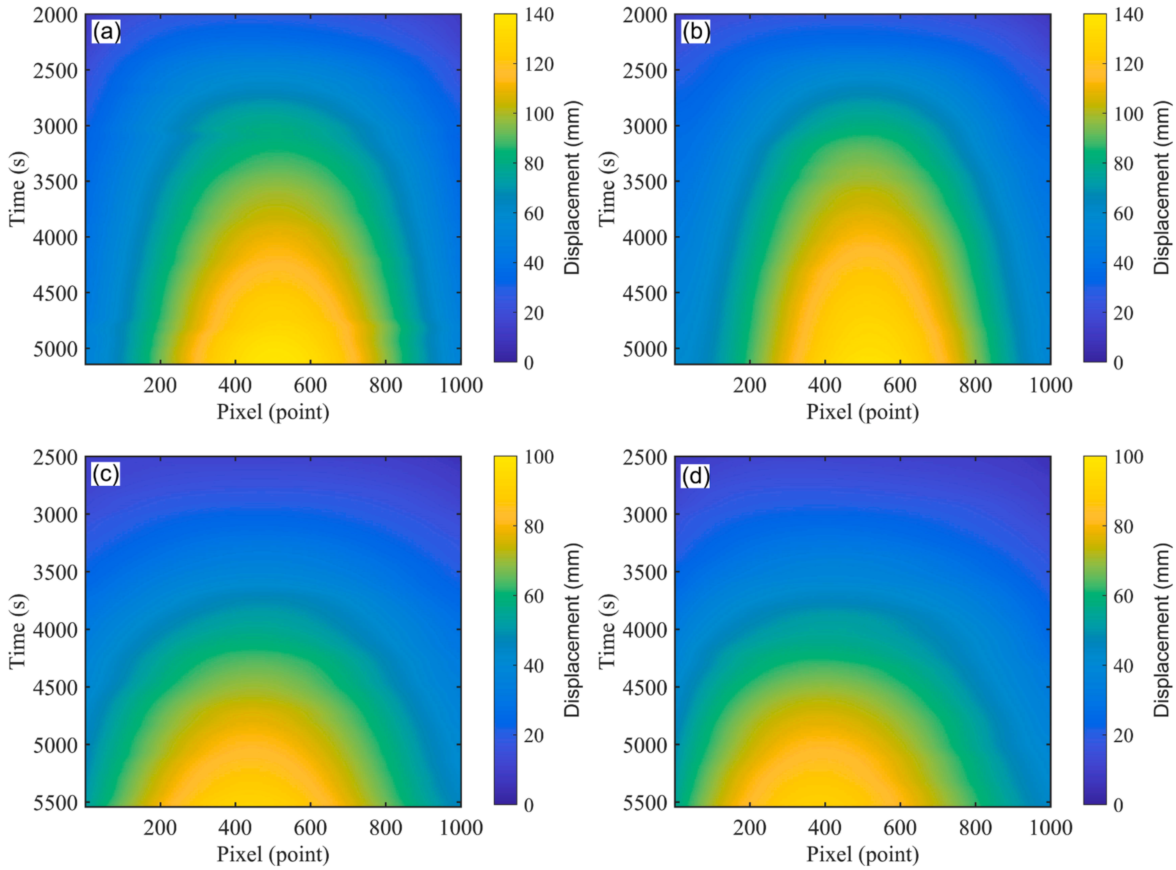

Fig. 15. Deformation measurement results (after RLOWESS optimization) for Experiment 0410 derived from (a) K-means and (b) U-Net. Deformation measurement results (after RLOWESS optimization) for Experiment 0414 derived from (c) K-means; (d) U-Net.

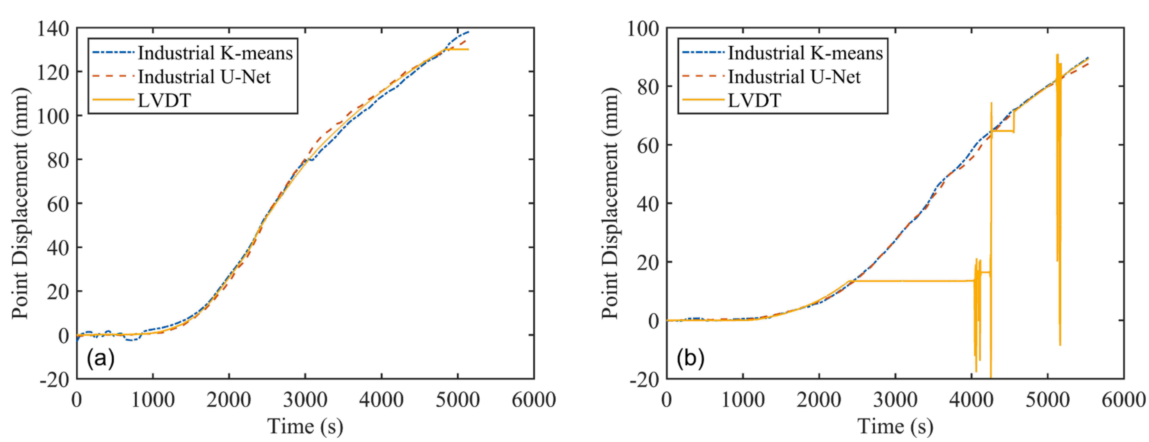

Fig. 16. Comparison between measurements derived from K-means, U-Net and LVDT for (a) Experiment 0410 and (b) Experiment 0414.

4. Discussion

4.1. The potentials of visual segmentation measurement method for RC column

In this paper, a non-contact measurement method based on visual segmentation is introduced to measure the deformation and displacement of the RC column with FRP tubes embedded in the concrete columns. This method offers accuracy comparable with the traditional LVDT measurements. The results demonstrate a relatively consistent and stable behavior during the visual measurement stage and process, with little visual measurement errors observed in the displacement measurement stage. These errors can be attributed to factors such as changes in environmental lighting, image noise, the presence of unknown personnel in the scene, and vibrations of RC column with FRP tube due to the prolonged duration of the experiment. To reduce the impact of these factors on measurement errors, it is recommended to incorporate the displacement sensors alongside the visual measurement method. This complementary approach, combining the visual measurement method with the traditional method, can further enhances the accuracy of the algorithm and effectively filters out noise in the measurements. By integrating both techniques, a more robust and reliable measurement system can be achieved, minimizing the potential for errors and improving the overall accuracy of the deformation and displacement measurements.

This visual measurement system described in this study not only enables measurement of deformation and displacement, but also includes target localization and recognition, allowing for measurement of global deformation of the experimental target. By leveraging visual recognition and localization techniques, the system can accurately capture the position and shape information of the experimental target, enabling precise measurement of its global deformation. This comprehensive measurement approach provides more comprehensive data that enhances the analysis and interpretation of experimental results. Furthermore, it holds great significance for studying the mechanical properties and structural behavior of materials, enabling deeper insights into their characteristics and performance. Taking the relationship between column height and deformation size as an example, an examination of the correlation between the height of the RC column with FRP tube and the deformation variables can be investigated, based on the observation results from the three sets of experiments (0410, 0412, and 0414). Given the incomplete datasets from the LVDT measurements, validation was executed using the maximum deformation values obtained from the visual measurements mentioned above. The relationship between the tube's height and the deformation can be described by a second-order polynomial fit, demonstrating a trend of positive correlation.

The advantages of visual measurement for specimen deformation are mainly reflected in the following aspects. Firstly, visual measurement employs a non-contact measurement method to measure specimen deformation within the visual range. Moreover, it exhibits good target recognition capability, particularly for the RC column with FRP tube. Secondly, in terms of global deformation analysis, visual measurement can offer a comprehensive solution that surpasses the capability of traditional displacement sensors. The comparison between the visual measurement and the LVDT measurement reveals that the maximum relative error of the K-means method in visual measurement is only 3.18 %, the U-Net method is 1.13 %, with an overall relative error that remains within an acceptable accuracy range. The comparison results suggest that the visual measurement can provide more accurate global deformation parameters, surpassing the contact-based displacement sensors in terms of global deformation measurement. Finally, the visual measurement system, consisting of ordinary industrial cameras and self-developed software, offers cost-effectiveness, ease of replication, and eliminates the need for additional LVDT. This not only reduces the complexity associated with installing LVDT sensors, but also helps to reduce overall experimental costs.

In the context of comparing previous research on image processing with DIC, which is widely used for displacement measurements through point-to-point analysis in many studies, the current research highlights a critical requirement: the need to scatter the deformed target. DIC often faces challenges in tracking deformation, especially in unprocessed environments where the texture of the target image is absent. In contrast, this study leverages a range of iterative optimization methods to segment and identify columns in complex settings, establishing a solid baseline. This approach significantly reduces the probability of tracking errors during deformation monitoring. Unlike the point-to-point measurement methods, this method demonstrates reduced tracking errors in environments without background processing, thereby enhancing accuracy. In such complex scenarios, the model presented in this study shows superior applicability.

4.2. Possible limitations

4.2.1. Camera pose

It is worth noting that the camera's position and orientation do have significant impact on the accuracy of the visual measurements. Optimal accuracy is achieved when the camera is positioned directly in front of the experimental specimen. When the camera's attitude and Line-of-Sight (LoS) deviates, it is necessary to consider the spatial coordinate system of the camera. This system is assumed with x as the horizontal axis coordinate, y as the vertical axis coordinate, z as the distance coordinate, and o as the origin coordinate (i.e. the initial camera coordinate), to maintain a shot of the global specimen throughout the entire process.

Assuming that the LVDT is in the negative coordinate system of the x-axis (left side of the image), the sample sensor data is gradually acquired as the camera pose is moved in the negative direction of the x-axis. In this scenario, image segmentation may broaden its range due to the feature similarity between the side and front columns. But since the deformation measurements are relatively variable and the deformation can be inferred from the boundary points. Conversely, when the camera shift positively along the x-axis, the change in the column boundary's relative position is observed, with minimal error impact in this case. Movement along the y-axis results in simple vertical shifts of measurement points, the error of this change is also insignificant. However, increasing the distance along the z-axis leads to a progressive increase in error. The measurement sensitivity is expected to decrease due to the pixel representation of the measurement point's distance enlarging with increased measurement distance. Furthermore, moving the camera along the x-axis, y-axis and z-axis introduces errors due to the changing representation in pixels. Though it can be mitigated through calibration and optimized by reprojection errors.

Additionally, during the axial compression test, the column mainly deflects in a two-dimensional direction, according to the characteristics of axial compression. Consequently, when the camera LoS is a non-perpendicular to the objection's movement direction, parallax errors may arise. The narrower the angle between the camera line and the sample surface, akin to the non-linear form of pulling the camera away from the shooting distance, the larger the expected error.

4.2.2. Shape of the specimen

In this experiment, although the tested specimen has a square cross-section, the method can also be applicable to columns with circular cross-sections. During an axial compression test, a column with a circular cross-section is likely to experience bending deformation, akin to that observed in square cross-section columns. Thus, the proposed method remains effective in such cases. The digital image processing technique used in this study captures edge information as curves following deformation, which are then refined through polynomial fitting. For circular cross-section columns, the primary view still appears rectangular. Displacement of the side edges alters the rectangle's shape, allowing for the extraction of corresponding deformation based on this alteration. In the case where the column is deflected in an unknown a-priori direction, one possible way to utilize the proposed approach is to place an additional camera perpendicular to the primary camera. This arrangement allows for the simultaneous capture of both frontal and lateral views of the specimen, providing a comprehensive analysis of the specimen's displacement in multiple dimensions. A multi-view (360-degree) monitoring approach could further enhance the detection capabilities for unpredictable deformation patterns if the monitoring site permits for the placement of multiple cameras. Moreover, employing binocular vision for accurate depth perception, although not included in this study, could be an alternative method for mapping deformations in the Z-direction of columns. The authors acknowledge the importance of these considerations and intend to explore these advanced techniques in future work to overcome the current limitations.

4.2.3. Sample size of training

This data for this study was semantically segmented using a database created from actual samples, resulting in 1006 data samples and their corresponding labels for training the semantic segmentation model. However, this approach presents certain limitations. Currently, accurate recognition and segmentation are only achievable for RC columns with FRP tubes. To overcome this limitation, it is necessary to gradually include more data samples featuring diverse characteristics. In the context of deep learning methods tailored for specific research objects, datasets are labeled for model evaluation and consideration. During the training process, these labeled datasets undergo preprocessing, such as rotation, flipping, and scaling the training images. These modification aim to increase the diversity of the dataset and the generalization ability of the model. Such approach is employed due to the lack of relevant large-scale datasets on this particular scenario. Looking forward, the goal is to establish a multi-sample public data platform, enabling more comprehensive research in this area.

4.2.4. Illumination

The potential impact of lighting variations on computer vision systems, especially in indoor settings, is a critical factor to consider. Changes in illumination can alter the image's contrast, brightness, and color, potentially affecting the performance of vision algorithms. In the actual experiments, a comparative analysis with the experimental results indicated that the influence of illumination changes was relatively minimal. Nonetheless, in future research, it is worth to place greater emphasis on the stability of the optical setup, recognizing it as a promising area of study. The goal is to enhance system stability under diverse lighting conditions through more precise optical adjustments, and continuously improve the robustness of the algorithm in real-world applications. Pursuing in-depth research in this direction is anticipated to significantly advance the performance of computer vision systems in environments with complex lighting conditions.

4.2.5. Memory space

The collection of video data may occupy a large amount of memory space, so in future measurements, low frame rate data collection methods can be considered to address this issue.

In summary, for accurate deformation measurement of a column, the camera should ideally have a direct, perpendicular LoS to the movement direction, adequate resolution, proper distance, and good lighting conditions.

4.3. Future prospects: expanding image processing applications in engineering

With the continuous evolution of computer vision and deep learning techniques, a more significant role is expected to be played by image processing in structural health monitoring. The optimization of the image segmentation-based deformation measurement method, aimed at enhancing its robustness and adaptability to a variety of structural morphologies, is anticipated. Furthermore, an extension of these research results to other engineering branches, such as bridge and building engineering, is planned, to broaden the application spectrum of image processing techniques in diverse engineering fields.

Specifically, in bridge engineering, the refined deformation measurement method could be utilized for routine inspections and the detection of structural damage. In the construction sector, the application of this enhanced technique is expected to expedite the identification of structural defects and damages.

Therefore, the implication of this work is not confined to monitoring deformation in RC columns alone; it encompasses a wide range of potential applications in several engineering fields. The focus of future work will be on the enhancement of the current methodology and the exploration of these diverse applications, to fully realize the potential of image processing in engineering.

5. Conclusions

This paper presents a novel method for dynamic image segmentation, recognition, and deformation measurement, designed specifically for axial compression experiments of the RC column with FRP tube. The image data, sourced from an in-house developed visual measurement system, serves the purpose of analyzing the deformation process of the RC column with FRP tube under axial compression. The method includes the entire process of image-based clustering segmentation and semantic segmentation recognition measurement, which involves the development of two distinct visual measurement methods procedures, each accompanied by calculation programs and enhancement of relevant algorithms. In addition, an improved full-field edge displacement fitting method is proposed for real-time identification and tracking of displacement targets, enabling displacement tracking measurement in complex dynamic environments. Through this algorithm, visual deformation and full-field displacement measurement are achieved. The proposed method successfully captures and visualizes the dynamic deformation process of the RC column with FRP tube, signifying its efficacy and potential utility in future applications.

In this research, the image segmentation and measurement system analyzed over 50,000 frames of images per experimental group, encompassing a total of nine groups, focusing on varies size of the RC column with FRP tube. The system generated an enhance image in every three frames, while gathering one displacement measurement sample per second, each experimental set needs to collect more than 4000 samples. Comparative analysis with displacement sensor data revealed that the average maximum standard deviation for the K-means method was 3.10 mm, maintaining overall relative errors within an acceptable accuracy range. The findings suggest that the clustering image segmentation-based visual measurement system can meet the dynamic measurement requirements of the RC column with FRP tube. The consistency between the measurement results from the clustering visual measurement system and the displacement sensor verifies the effectiveness of the clustering visual measurement system algorithm.

Similarly, semantic segmentation generates an enhanced image every three frames, while gathering one displacement measurement sample per second, each experimental set needs to collect more than 4000 samples. When compared to the displacement meter data, the average maximum standard deviation of the U-Net method is 1.78 mm, with the overall relative error maintained within an acceptable accuracy range. The results demonstrate that the visual measurement system, based on semantic image segmentation and its corresponding algorithm program, can meet the dynamic measurement requirements of the RC column with FRP tube. The measurement results are consistent with the actual displacement meter readings, demonstrating the effectiveness of the semantic image segmentation-based visual measurement system algorithm program.

The result shows that the adoption of the two discussed visual measurement systems can either supplement or replace the contact-based displacement sensor measurement method, offering a non-contact measurement approach that can partially mitigate issues commonly associated with the physical contact-based measurement methods, such as sticking or exceeding the measurement range. The experiments conducted in this research have demonstrated that these two images segmentation-based visual measurement systems yield effective global measurement validation data and maintain reliable accuracy. The average relative errors of the two visual measurement methods for full-field deformation are 1.03 % and 0.44 %, respectively. While image noise and environment factors during visual measurement may introduce some errors, the overall correlation between the concrete deformation signal and the displacement sensor remains high, with a minimal overall measurement error, thereby assuring confidence in global visual measurement approach.

The visual measurement method proposed in this work is not only applicable for global deformation analysis in axial compression experiments, but have great potential in extending its applicability to large-scale structures and buildings, and providing reliable data in complex dynamic environments. Moreover, it can provide reliable measurement data in complex dynamic environments. However, its performance may be influenced by lighting and environmental factors in extreme environments. Therefore, the selection of suitable image pre-processing algorithms and coefficients become crucial, as does determining the size and position of filtering windows when occlusions occur. In a follow-up study, extending the dataset and following up with new models can help to build models with wider applicability and higher accuracy; The use of 3D deformation monitoring allows for more complete deformation data as well as providing validation for out-of-place; when large scene measurements are encountered, simultaneous localization and mapping buildup measurements would be a solution. These considerations are essential for constructing a high-quality visual measurement model that remains effective under a variety of conditions.

CRediT authorship contribution statement

Yankang Zhai: Writing – review & editing, Writing – original draft, Visualization, Validation, Software, Methodology, Investigation, Formal analysis, Conceptualization. **Alex Hay-Man Ng:** Writing – review & editing, Visualization, Validation, Methodology, Investigation, Formal analysis, Conceptualization, Resources, Supervision. **Zhenpeng Luo:** Validation, Investigation, Data curation. **Jiahui Wang:** Validation, Investigation, Data curation. **Lijuan Li:** Writing – review & editing, Supervision, Project administration, Methodology, Funding acquisition, Conceptualization. **Zhe Xiong:** Writing – review & editing, Supervision, Resources, Investigation, Data curation. **Hua Wang:** Writing – review & editing, Supervision, Methodology, Investigation.

Declaration of competing interest

The authors declare that they have no known competing financial interests or personal relationships that could have appeared to influence the work reported in this paper.

Data availability

Data will be made available on request.

Acknowledgments

This research was funded by the Program for Guangdong Introducing Innovative and Entrepreneurial Teams (2019ZT08L213), National Natural Science Foundation of China (Project No. 12032009), and the Science and Technology Planning Project of Guangzhou City (Project No. 202002030120).

Appendix A. Supplementary data

Supplementary data to this article can be found online at https://doi.org/10.1016/j.measurement.2024.114207.

References

[1] D. Shi, Q. Shi, Study on mechanical properties and mesoscopic numerical simulation of recycled concrete, Sustain. 14 (19) (2022) 12125.
[2] D.E. Nassani, Experimental and analytical study of the mechanical and flexural behavior of hybrid fiber concretes, Structures. 28 (2020) 1746–1755.
[3] S. Joshi, S.M. Harle, Linear variable differential transducer (LVDT) & its applications in civil engineering, Int. J. Transp. Eng. Technol. 3 (4) (2017) 62–66.
[4] F. Tang, Z. Li, Y. Tang, Y. Chen, H.-N. Li, Simultaneous measurement of shrinkage and coefficient of thermal expansion of mortar based on EFPI sensors with nanometer resolution, Measurement 152 (2020) 107376.
[5] S. Shiming, S. Yupu, Dynamic biaxial tensile–compressive strength and failure criterion of plain concrete, Constr. Build. Mater. 40 (2013) 322–329.
[6] E. Bicici, H. Sezen, Cyclic shear displacement model for reinforced concrete columns, Eng. Struct. 247 (2021) 113211.
[7] E. Bicici, H. Sezen, Cyclic displacement model for reinforced concrete columns, Earthq. Eng. Struct. Dyn. 52 (1) (2023) 71–87.
[8] H. Mandal, S.K. Bera, S. Saha, P.K. Sadhu, S.C. Bera, Study of a modified LVDT type displacement transducer with unlimited range, IEEE Sens. J. 18 (23) (2018) 9501–9514.
[9] S. Karunarathna, S. Linforth, A. Kashani, X. Liu, T. Ngo, Effect of recycled rubber aggregate size on fracture and other mechanical properties of structural concrete, J. Clean. Prod. 314 (2021) 128230.
[10] T. Xing, et al., High accuracy measurement of heterogeneous deformation field using spatial-temporal subset digital image correlation, Measurement 156 (2020) 107605.
[11] Y.-C. Tang, L.-J. Li, W.-X. Feng, F. Liu, X.-J. Zou, M.-Y. Chen, Binocular vision measurement and its application in full-field convex deformation of concrete-filled steel tubular columns, Measurement 130 (2018) 372–383.
[12] Y. Zhou, Q. Li, L. Chu, Y. Ma, J. Zhang, A measurement system based on internal cooperation of cameras in binocular vision, Meas. Sci. Technol. 31 (6) (2020) 065002.
[13] R. Cong, J. Lei, H. Fu, M.-M. Cheng, W. Lin, Q. Huang, Review of visual saliency detection with comprehensive information, IEEE Transactions on Circuits and Sys. for Video Technol. 29 (10) (2018) 2941–2959.
[14] Q. Wu, F. Hu, A. Zhu, Z. Wang, Y. Bao, Learning spatial–temporal features via a pose-flow relational model for action recognition, AIP Adv. 10 (7) (2020) 075208.
[15] Z. Lin, H. Shang, H. Gao, X. Huang, In Situ Measurement of the strain field at the fatigue crack tip based on sub-image stitching and matching DIC, Materials. 15 (15) (2022) 5150.
[16] B. Zhou, Y. Li, L. Wang, H. Jia, X. Zeng, The role of grain boundary plane in slip transfer during deformation of magnesium alloys, Acta Mater. 227 (2022) 117662.
[17] Z. Dong, Y. Li, L. Jiao, W. Zhang, Y. Liu, D. Peng, Pressure-sensitive paint integrated with digital image correlation for instantaneous measurement on rotating blades, Aerosp. Sci. Technol. 126 (2022) 107667.
[18] Y. Zhu, S. Wang, T. Liu, C. Liu, X. Liu, A visual measurement method of structural body vibration displacement combined with image deblurring, Measurement 211 (2023) 112598.
[19] C. Fang, X. Fan, H. Zhong, L. Lombardo, H. Tanyas, X. Wang, A Novel historical landslide detection approach based on LiDAR and lightweight attention U-Net, Remote Sens. (Basel). 14 (17) (2022) 4357.
[20] G. Nsengiyumva, Y. Kim, Field displacement-based inverse method for elastic and viscoelastic constitutive properties, Exp. Mech. 62 (9) (2022) 1553–1568.
[21] M.-N. Wu, C.-C. Lin, C.-C. Chang, Brain tumor detection using color-based k-means clustering segmentation, in: Third international conference on intelligent information hiding and multimedia signal processing (IIH-MSP 2007). 10 (2007) 245-250.
[22] S. Yadav, M. Biswas, Improved color-based K-mean algorithm for clustering of satellite image, in: 2017 4th International Conference on Signal Processing and Integrated Networks (SPIN) 10 (2017) 468–472.
[23] A.F.M. Musa, D.Q. Utama, Segmentation image re-coloring based on K-means clustering algorithm as a tool for partial color-blind people, J. Phys. Conf. Ser. 1192 (2019) 012012.
[24] J. Shang, et al., Automatic pixel-level pavement sealed crack detection using multi-fusion U-net network, Measurement 208 (2023) 112475.
[25] O. Ronneberger, P. Fischer, T. Brox, U-net: Convolutional networks for biomedical image segmentation, Medical Image Computing and Computer-Assisted Intervention–MICCAI 10 (2015) 234–241.
[26] H. Guo, D. Yang, PRDNet: medical image segmentation based on parallel residual and dilated network, Measurement 173 (2021) 108661.
[27] N.A.M. Isa, S.A. Salamah, U.K. Ngah, Adaptive fuzzy moving K-means clustering algorithm for image segmentation, IEEE Trans. Consum. Electron. 55 (4) (2009) 2145–2153.
[28] A. Nithya, A. Appathurai, N. Venkatadri, D. Ramji, C.A. Palagan, Kidney disease detection and segmentation using artificial neural network and multi-kernel K-means clustering for ultrasound images, Measurement 149 (2020) 106952.
[29] L. Chen, W. Shan, P. Liu, Identification of concrete aggregates using K-means clustering and level set method, Structures. 34 (2021) 2069–2076.
[30] V. Hemamalini, et al., Food quality inspection and grading using efficient image segmentation and machine learning-based system, J. Food Qual. 10 (2022) 1–6.
[31] J. Zhang, X. Zhao, Z. Chen, Z. Lu, A review of deep learning-based semantic segmentation for point cloud, IEEE Access. 7 (2019) 179118–179133.
[32] X. He, Y. Zhou, J. Zhao, D. Zhang, R. Yao, Y. Xue, Swin transformer embedding U-Net for remote sensing image semantic segmentation, IEEE Trans. Geosci. Remote Sens. 60 (2022) 1–15.
[33] B. Dai, et al., A novel method for extracting time series information of deformation area of a single landslide based on improved U-Net neural network, Front. Earth Sci. 9 (2021) 785476.
[34] I. Qureshi, et al., Medical image segmentation using deep semantic-based methods: A review of techniques, applications and emerging trends, Information Fusion. 90 (2023) 316–352.
[35] J. Baili, et al., Experiments and predictive modeling of optimized fiber-reinforced concrete columns having FRP rebars and hoops, Mech. Adv. Mater. Struct. 30 (23) (2023) 4913–4932.
[36] D. Ershov, et al., TrackMate 7: integrating state-of-the-art segmentation algorithms into tracking pipelines, Nat. Methods. 19 (7) (2022) 829–832.
[37] Y. Li, Research and application of deep learning in image recognition, in: 2022 IEEE 2nd International Conference on Power, Electronics and Computer Applications (ICPECA), 10 (2022) 994–999.
[38] X.-X. Yin, L. Sun, Y. Fu, R. Lu, Y. Zhang, U-Net-Based medical image segmentation, J. Healthcare Eng. 10 (2022) 4189781.
[39] Q. Zhang, Y. Zhou, Recent advances in non-Gaussian stochastic systems control theory and its applications, Int. J. Network Dynamics and Intell. 1 (1) (2022) 111–119.
[40] B. Shan, S. Zheng, J. Ou, A stereovision-based crack width detection approach for concrete surface assessment, KSCE J. Civ. Eng. 20 (2016) 803–812.
[41] K. Ito, K. Xiong, Gaussian filters for nonlinear filtering problems, IEEE Trans. Autom. Control. 45 (5) (2000) 910–927.

[42] S. Wang, F. Wu, P. Takyi-Aninakwa, C. Fernandez, D.-I. Stroe, Q. Huang, Improved singular filtering-Gaussian process regression-long short-term memory model for whole-life-cycle remaining capacity estimation of lithium-ion batteries adaptive to fast aging and multi-current variations, Energy. 284 (2023) 128677.
[43] R.O. Julio, L.B. Soares, E. Costa, S. Bampi. Energy-efficient Gaussian filter for image processing using approximate adder circuits 1109, 2015, pp. 450–453.
[44] Z. Zhang, J. Hou, Q. Ma, Z. Li, Efficient video frame insertion and deletion detection based on inconsistency of correlations between local binary pattern coded frames, Security and Communication Networks. 8 (2) (2015) 311–320.
[45] J. Liu, Y. Zhang, Q. Zhao, Video stabilization algorithm based on Pearson correlation coefficient, in: 2019 International Conference on Advanced Mechatronic, Systems (ICAMechS). 10 (2019) 289-293.
[46] A. Ramirez, H. Arguello, G.R. Arce, Anomaly recovery from compressed spectral imagery via low-rank matrix minimization, in Independent Component Analyses, Wavelets, Neural Networks, Biosystems, and Nanoengineering IX. 8058 (2011) 66–71.
[47] A.A. Mohamed, F. Alqahtani, A. Shalaby, A. Tolba, Texture classification-based feature processing for violence-based anomaly detection in crowded environments, Image Vis. Comput. 124 (2022) 104488.
[48] M.A. Azam, et al., A review on multimodal medical image fusion: compendious analysis of medical modalities, multimodal databases, fusion techniques and quality metrics, Comput. Biol. Med. 144 (2022) 105253.
[49] D. Rukhovich, et al., Maps of averaged spectral deviations from soil lines and their comparison with traditional soil maps, Eurasian Soil Sci. 49 (2016) 739–756.
[50] K. Wikantika, S. Uchida, Y. Yamamoto, An evaluation of the use of integrated spectral and textural features to identify agricultural land cover types in Pangalengan, West Java, Indonesia, Japan Agricultural Research Quarterly: JARQ. 38 (2) (2004) 137–148.
[51] S. Liu, B. Yang, Y. Wang, J. Tian, L. Yin, W. Zheng, 2D/3D multimode medical image registration based on normalized cross-correlation, Appl. Sci. 12 (6) (2022) 2828.
[52] Z. Zhou, X. Zhao, S. Zhu, K-harmonic means clustering algorithm using feature weighting for color image segmentation, Multimed. Tools Appl. 77 (2018) 15139–15160.
[53] X. Shasha, L. Wenbin, K. Feng, Z. Yongjun, L. Yubin, Evaluation of grapevine sucker segmentation algorithms for precision targeted spray, Int. J. Agric. Biol. Eng. 8 (4) (2015) 77–85.
[54] X. Yu, et al., Maize tassel area dynamic monitoring based on near-ground and UAV RGB images by U-Net model, Comput. Electron. Agric. 203 (2022) 107477.
[55] L. Dong, W. Zhang, W. Xu, Underwater image enhancement via integrated RGB and LAB color models, Signal Process. Image Commun. 104 (2022) 116684.
[56] A.G. Wee, D.T. Lindsey, S. Kuo, W.M. Johnston, Color accuracy of commercial digital cameras for use in dentistry, Dent. Mater. 22 (6) (2006) 553–559.
[57] R. Bello-Cerezo, F. Bianconi, A. Fernández, E. González, F. Di Maria, Experimental comparison of color spaces for material classification, J. Electron. Imaging. 25 (6) (2016) 061406.
[58] M. Syakur, B. Khotimah, E. Rochman, B.D. Satoto, Integration k-Means Clustering Method and Elbow Method for Identification of the Best Customer Profile Cluster, IOPScience 336 (2018) 012017.
[59] X. Wang, Y. Bai, The global Minmax K-means algorithm, Springerplus. 5 (1) (2016) 1–15.
[60] M. Chen, C.J. Yin, Y.P. Xi, A new clustering algorithm partition K-means, Engineering Materials, Trans Tech Publ. 474 (2011) 577–580.
[61] A.M.G. Allah, A.M. Sarhan, N.M. Elshennawy, Edge U-Net: brain tumor segmentation using MRI based on deep U-Net model with boundary information, Expert Syst. Appl. 213 (2023) 118833.
[62] S. Zhang, C. Zhang, Modified U-Net for plant diseased leaf image segmentation, Comput. Electron. Agric. 204 (2023) 107511.
[63] Y. Guo, X. Duan, C. Wang, H. Guo, Segmentation and recognition of breast ultrasound images based on an expanded U-Net, PLoS One 16 (6) (2021) e0253202.
[64] A. Torralba, B.C. Russell, J. Yuen, Labelme: Online image annotation and applications, Proc. IEEE. 98 (8) (2010) 1467–1484.
[65] F. Merchant, K. Castleman, Microscope image processing, Academic press, 2022.
[66] X. Zhang, H. Yuan, Edge detection of printed matter based on improved Canny operator, in: 2022 IEEE 10th Joint International Information Technology and Artificial Intelligence Conference (ITAIC) 10, 2022, pp. 2546–2549.
[67] S. Aftab, R.H. Moghadam, Robust data smoothing algorithms and wavelet filter for denoising sonic log signals, J. Appl. Geophys. 206 (2022) 104836.
[68] M.G. Bruno, G. Marcelo, Sequential monte carlo methods for nonlinear discrete-time filtering, Springer Nature, 2022.
[69] Q. Chen, Q.-S. Sun, P.A. Heng, D.-S. Xia, A double-threshold image binarization method based on edge detector, Pattern Recogn. 41 (4) (2008) 1254–1267.
[70] F.Y. Shih, Image processing and mathematical morphology: fundamentals and applications, CRC Press, 2009.
[71] M. Versaci, F.C. Morabito, Image edge detection: a new approach based on fuzzy entropy and fuzzy divergence, Int. J. Fuzzy Syst. 23 (4) (2021) 918–936.
[72] D. Sangeetha, P. Deepa, FPGA implementation of cost-effective robust Canny edge detection algorithm, J. Real-Time Image Proc. 16 (2019) 957–970.
[73] W. Yu, L. Wang, Anderson's claim on fourth-order SPR synthesis is true, IEEE Transactions on Circuits and Systems i: Fundamental Theory and Applications 48 (4) (2001) 506–509.
[74] E. Dubois, S. Sabri, Noise reduction in image sequences using motion-compensated temporal filtering, IEEE Trans. Commun. 32 (7) (1984) 826–831.
[75] K. Malek, F. Moreu, Realtime conversion of cracks from pixel to engineering scale using Augmented Reality, Autom. Constr. 143 (2022) 104542.
[76] N.J. Singh, K. Nongmeikapam, Semantic segmentation of satellite images using deep-UNet, Arab. J. Sci. Eng. 48 (2) (2023) 1193–1205.
[77] X. Zhang, H. Liu, M. Che, Z. Geng, Y. Jiu, Research on Displacement Measurement and Self-detecting Circuit Based on LVDT, J. Phys. Conf. Ser. 2437 (2023) 01215.
[78] M. Ghyabi, et al., Vision-based measurements to quantify bridge deformations, J. Bridg. Eng. 28 (1) (2023) 05022010.